

Exp Astron (2016) 42:101–138
DOI 10.1007/s10686-016-9496-z



ORIGINAL ARTICLE

Towards practical autonomous deep-space navigation using X-Ray pulsar timing

Setnam Shemar¹ · George Fraser² · Lucy Heil³ ·
David Hindley¹ · Adrian Martindale² ·
Philippa Molyneux² · John Pye² ·
Robert Warwick² · Andrew Lamb⁴

Received: 16 March 2016 / Accepted: 1 April 2016 / Published online: 30 July 2016

© The Author(s) 2016. This article is published with open access at Springerlink.com

Abstract We investigate the feasibility of deep-space navigation using the highly stable periodic signals from X-ray pulsars in combination with dedicated instrumentation on the spacecraft: a technique often referred to as ‘XNAV’. The results presented are based on the outputs from a study undertaken for the European Space Agency. The potential advantages of this technique include increased spacecraft autonomy and lower mission operating costs. Estimations of navigation uncertainties have been obtained using simulations of different pulsar combinations and navigation strategies. We find that the pulsar PSR B1937+21 has potential to allow spacecraft positioning uncertainties of ~2 and ~5 km in the direction of the pulsar after observation times of 10 and 1 h respectively, for ranges up to 30 AU. This could be achieved autonomously on the spacecraft using a focussing X-ray instrument of effective area ~50 cm² together with a high performance atomic clock. The Mercury Imaging X-ray Spectrometer (MIXS) instrument, due to be launched on the ESA/JAXA BepiColombo mission to Mercury in 2018, is an example of an instrument that may be

GF deceased 18 March 2014

✉ Setnam Shemar
setnam.shemar@npl.co.uk

✉ John Pye
pye@leicester.ac.uk

¹ National Physical Laboratory, Hampton Road, Teddington, Middlesex TW11 0LW, UK

² Department of Physics and Astronomy, University of Leicester, University Road, Leicester LE1 7RH, UK

³ Anton Pannekoek Institute for Astronomy, University of Amsterdam, Postbus 94249, Amsterdam, GE 1090, The Netherlands

⁴ UK National Quantum Technology Hub in Sensors and Metrology, School of Physics and Astronomy, University of Birmingham, Birmingham B15 2TT, UK

further developed as a practical telescope for XNAV. For a manned mission to Mars, where an XNAV system could provide valuable redundancy, observations of the three pulsars PSR B1937+21, B1821-24 and J0437-4715 would enable a three-dimensional positioning uncertainty of ~30 km for up to 3 months without the need to contact Earth-based systems. A lower uncertainty may be achieved, for example, by use of extended observations or, if feasible, by use of a larger instrument. X-ray instrumentation suitable for use in an operational XNAV subsystem must be designed to require only modest resources, especially in terms of size, mass and power. A system with a focussing optic is required in order to reduce the sky and particle background against which the source must be measured. We examine possible options for future developments in terms of simpler, lower-cost Kirkpatrick-Baez optics. We also discuss the principal design and development challenges that must be addressed in order to realise an operational XNAV system.

Keywords XNAV · Spacecraft · Navigation · Pulsar · X-ray · Timing

1 Introduction

The navigation of deep space missions is currently achieved by the ESA's European Space Tracking (ESTRACK) network and NASA's Deep Space Network (DSN) [18]. Each of these employ a global network of large ground-based radio antennas. In recent years space agencies around the world have been exploring the feasibility of using X-ray pulsars for spacecraft navigation. Whereas the DSN and ESTRACK networks require a spacecraft to communicate with ground-based systems, the use of pulsars would to some extent enable autonomous navigation on-board the spacecraft thereby minimising communications with Earth. This would also offer the potential of lower mission operating costs due to the reduced need for ground infrastructure.

Pulsars are ultra-compact, rapidly rotating and strongly magnetised neutron stars that are the remnants of the death of a massive star in a supernova explosion [50]. The high timing stability of the pulses from certain types of pulsars has led to important developments including strong evidence for the existence of gravitational waves [80]. It was first speculated that pulsars could be used for time and position determination for spacecraft by Reichley et al. [63] and Downs [22]. Chester and Butman [14] described the potential use of X-ray pulsars for spacecraft navigation due to the much smaller detector size required compared to that for radio pulsars (see also review by [8]).

The main objective of the work presented here was to investigate the feasibility of deep space navigation using XNAV based on X-ray pulsars from a high-level perspective considering also the X-ray instrumentation. Section 2 provides a brief review of literature on pulsar-based navigation concepts relevant to this study. In Section 3 we present a catalogue of X-ray pulsars that are potentially suitable for the navigation concepts and some of their relevant characteristics and parameters. Section 4 analyses the potential Position, Velocity and Time (PVT) estimation errors that can be obtained using different combinations of X-ray pulsars and navigation strategies. In Section 5 we describe the X-ray instrumentation technology that is currently available for use in an XNAV system as well as potential future developments. Section 6 discusses the performance and limitations of an XNAV system and compares these to those of the ESTRACK and DSN networks. Finally, in Section 7 we give the conclusions.

2 Relevant concepts for navigation

This technique is based on ranging and velocity estimation by use of pulsar timing and frequency measurements. For a given pulsar, the time interval between pulses is referred to as the pulse period, P , and this generally changes slowly and uniformly with time. The pulse periods of different pulsars can range between 1.5 ms and several seconds. Here we firstly describe the measurement of pulse Times-Of-Arrival (TOAs, see e.g. [48], Section 8.1) and the processing necessary for such a system together with the pulsar timing models. We then focus on navigation strategies suitable for PVT estimation.

We briefly review here the main aspects directly relevant to our study; the reader is referred to the published literature (e.g. [34, 69]) for a more extensive view. In particular, we restrict ourselves to consideration of two navigation methods (utilising one pulsar and three or four pulsars) and the periodic signal from rotation-powered X-ray pulsars.

2.1 Pulse timing

One of the most important requirements for such a system is for the spacecraft to have access to a reliable timing model for the pulsar. The most accurate models are often derived from radio observations on Earth. The pulse phase of a pulsar can be modelled and specified at a known location, for example the Solar System Barycentre (SSB), using the measured pulse phase and pulse frequency of the pulsar at a given epoch [48, 50, 69]. The model will not be perfect since the exact values of pulse phase, pulse frequency and derivatives will not be known and the TOAs will be affected by measurement error. Furthermore, some pulsars can also exhibit significant timing irregularities called ‘timing noise’ (e.g. [39]) and ‘glitches’ (e.g. [25, 71]) which are intrinsic to the rotation of a star.

An X-ray instrument on-board the spacecraft is used to obtain time-resolved measurements of a given pulsar. Pulse TOAs are then extracted by comparing the measured time-series with a model pulse profile [24, 31, 36, 68]. Figure 1 (see also Section 2.2.1) shows lines representing a given pulse phase of a pulsar signal arriving at the true spacecraft position and an initial estimate of the position at two instants in time, separated by an interval Δt , as the signal moves through the Solar System relative to the inertial reference frame of the SSB [69]. In the simplest case, the pulse TOAs measured at the spacecraft are compared with those predicted at the SSB by the timing model in order to obtain a corrected spacecraft position estimate along the direction of the pulsar. This requires conversion of the measured TOAs to Barycentric TOAs, using the initial position estimate and the unit vector to the pulsar, \hat{n} , with respect to the SSB [69]. These are the key pulsar timing elements that enable positioning of the spacecraft in the direction of a given pulsar.

2.2 Navigation

Here we describe some navigation strategies suitable for PVT estimation. These can be categorized as *delta-correction* and *absolute navigation* techniques [34] and will be discussed in turn below. In all cases it is necessary that the pulsar timing models for

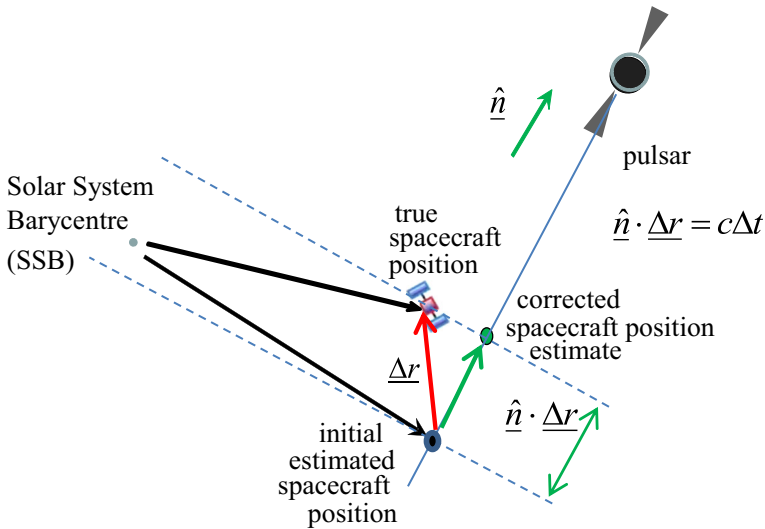


Fig. 1 A simplified approach for measuring the position of a spacecraft in the direction of a pulsar. The dashed lines represent a given pulse phase of a signal from the pulsar arriving at the true spacecraft position and an initial estimated position at two instants in time separated by an interval Δt . The ‘delta-correction’ is shown as $\hat{n} \cdot \Delta r$ and is equal to $c\Delta t$, where c is the speed of light. The green point represents the corrected spacecraft position along the direction of the pulsar

relevant pulsars are updated sufficiently frequently within the XNAV processing system such that the errors arising from these do not contribute significantly to the navigation uncertainties. These updates would be carried out for example using the ESTRACK or DSN networks, whilst the interval between updates would depend on the pulsars employed, but could vary for example between one update per day to a year.

2.2.1 Delta-correction measurement using a single pulsar

This is the simplest strategy and represented in Fig. 1. A more detailed description of this can be found in [34, 69]. An initial estimate of the spacecraft position is required to within $cP/2$, where c is the speed of light, as well as an estimate of the velocity. These might be obtained using for example the DSN, ESTRACK or an orbit propagation process within the spacecraft navigation system [69]. An accurate time reference on-board the spacecraft enables measurement of the observed pulse TOAs from a single pulsar. If the initial spacecraft position estimate used to convert the TOAs to the SSB is correct and there are no TOA measurement errors then there will be no time-offset, Δt , compared to the TOAs predicted by the pulsar’s timing model. However, if the initial position estimate is in error then a non-zero time-offset, Δt , will be measured corresponding to a position-offset in the direction of the pulsar, $\hat{n} \cdot \Delta r = c\Delta t$, where \hat{n} is the unit vector to the pulsar with respect to the SSB and Δr is the error in the initial position estimate [69]. This position-offset is often referred to as the ‘delta-correction’ and enables a corrected spacecraft position estimate along the direction of the pulsar to be obtained. This strategy is relatively simple to implement as it requires an X-ray instrument that observes only a single pulsar at a time. It can, in principle, be extended to sequential observations of multiple pulsars to obtain two- or three-dimensional

position estimates although it would depend on the motion of the spacecraft and being able to adequately take account of this [69].

2.2.2 Absolute navigation

This strategy offers the potential for a spacecraft to autonomously determine its absolute position in three dimensions with respect to an inertial reference frame [69, 70]. The advantage of this is that it can navigate and restart without the aid of another method such as DSN. As shown in Fig. 2, by using measurements of pulse phase from four or more sources it would also be possible to measure and correct for any spacecraft clock time-offset. Alternatively three pulsars could be used if a high-accuracy time reference is available on-board the spacecraft, for example using a high-performance atomic clock. A difficulty arises because a pulsar signal does not include information to identify the number of the particular pulse received. This results in pulse or cycle ambiguities, a problem that can be overcome by combining the measured pulse phase information of several pulsars and using knowledge of the unit vector of each in order to identify the unique set of cycles that satisfies the measurements [69]. A priori knowledge such as an approximate location of the spacecraft within the Solar System and an estimate of the spacecraft velocity together with observations of longer period pulsars may initially be required in order to reduce the parameter search space [68].

Absolute navigation would in principle be the most versatile for many types of space missions depending on its performance. A disadvantage is that it requires simultaneous observations of multiple pulsars which would require multiple detectors, making this strategy more difficult to implement. Whether or not it would be possible to use data taken sequentially for different pulsars using a single detector would depend on the motion of the spacecraft and being able to adequately take account of this (Deng et al.

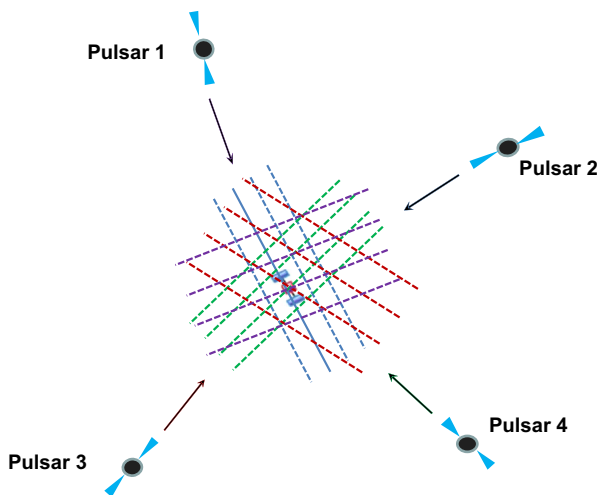


Fig. 2 Absolute navigation using simultaneous observations of a minimum of four pulsars enabling measurement of the spacecraft three-dimensional position (x, y, z) and the on-board clock time-offset, t_c , from terrestrial time scales. The dashed lines represent candidate lines of position for each pulsar separated by cP in each case and obtained using the measured pulse phases of the four pulsars at a given time

[21]). The noise in the spacecraft clock is unlikely to significantly degrade the quality of such sequential observations spanning over periods of 1 h to 1 day. This is because a relatively modest performance oscillator with a stability of 10^{-12} for averaging times of 1 day will lead to a range measurement error contribution of 30 m which is small compared to other error sources. An atomic oscillator of such a performance should be readily achievable on a spacecraft. Furthermore, with careful design, a quartz-based oscillator could be expected to exhibit a similar performance [11].

2.2.3 Determining velocity

An accurate approach for spacecraft velocity measurement involves comparing the frequency, or the rate, of pulses received at the spacecraft from one or more pulsars with those predicted at the SSB [69]. Any relative velocity between the pulsar and spacecraft will result in the interval between the received pulses either decreasing or increasing due to the Doppler Shift. After correcting for any motion of the pulsar relative to the SSB, any Doppler shift observed in the pulse timing has to be due to the motion of the spacecraft in the direction of the pulsar. By taking measurements from multiple pulsars it is possible to obtain velocity components of the spacecraft in three dimensions.

3 X-ray pulsars and their characteristics

We present the available X-ray pulsars and their characteristics, including their sky-position (i.e. astrometric) uncertainties. We also describe a simple analytical approach to estimate spacecraft range error, parameterised in terms of the pulsar properties and X-ray measurements, and compare this with results from simulations of detailed pulse profiles.

3.1 Compiling an X-ray pulsar catalogue for XNAV

There are over 2000 known pulsars, most of which were discovered in the radio band [52]. Approximately 100 of these are Rotation-Powered X-Ray Pulsars (RP-XRPs) [7], with around 35 of these having been detected with pulsed X-ray emission and having a measured pulse profile, as reported in the literature to ~mid-2012 – the ‘census epoch’ of our study. These XRPs, which have rotation periods ranging from ~1.5 to 100 s of milliseconds [7], are the main focus of this work. Accretion-powered pulsars (see e.g. [7]), are rather poor in terms of pulse stability (and some are unsuitable as they are highly transient in flux, and some have rather long periods, of seconds or greater), though they may have some utility provided there are associated X-ray monitoring observations from a low-Earth orbit satellite.

The majority of the rotation-powered pulsar population are relatively bright and young with ages $\sim 10^3$ to $\sim 10^7$ yr [7]; the most famous example of which is the Crab pulsar (PSR B0531+21), born in AD 1054. A relatively small fraction can exhibit extremely high long-term timing stability – excellent attributes for a ‘celestial clock’ [10, 24, 69]. These are the ‘MilliSecond Pulsars’ (MSPs) which have the shortest periods and are relatively weak in strength. They are relatively old objects with ages of typically $\sim 10^7$ to $\sim 10^{10}$ yr (see [7], Fig. 6.2). However, young pulsars such as the Crab

may also be useful if monitored sufficiently frequently from the ground (in radio) or from an X-ray monitoring satellite. Of order 10 % of all known pulsars are MSPs; however, they constitute ~50 % of known rotation-powered X-ray pulsars, and ~30 % of those with detected pulsed emission in X-rays [7].

With the exception of the Crab pulsar which is one of the brightest X-ray sources in the sky, other known rotation-powered pulsars have X-ray fluxes measured at the Earth typically a thousand times fainter. Even then only a small number of sources (~3) are detected at the ‘milli-Crab’ level, with the rest being at least a factor of 5–10 fainter still.

General X-ray source catalogues such as those from ROSAT [76, 77], XMM-Newton [78] and Chandra [26] are available for pulsar X-ray source fluxes, whilst general astronomical object catalogues such as CDS SIMBAD¹ provide information on general source properties and categorisation. Furthermore, the ATNF pulsar ‘master’ catalogue² [52] provides detailed pulsar ephemerides and celestial coordinates.

The starting point for generation of a catalogue of relevant properties of RP-XRPs were the tabulations in Becker’s [7] review (these list 89 objects), together with the other databases mentioned above. These were augmented and updated from published literature (e.g. [30, 66]); in particular, the X-ray pulse width and fractional pulsed signal had to be extracted for each individual pulsar. A catalogue was compiled comprising data on 89 RP-XRPs, with the most detailed information being provided for the 35 RP-XRPs for which pulsed X-ray emission profiles were found in the literature. Table 1 lists some parameters for the 35 RP-XRPs with detected pulsations, including source flux,³ fractional pulse width, astrometric position error and estimates of the spacecraft range error contributions for ‘focussing’ and ‘collimated’ instrument types. The objects are ordered by increasing range error for a focussing instrument. The given range errors represent 1-sigma and are computed according to the analytic formula in Eq. A.3 (see also Section 3.3.1) using an observation time, $T_{\text{obs}} = 5 \times 10^3$ s, and instrument effective area, $A_{\text{eff}} = 0.005$ m², according to an ‘improved Point Spread Function (PSF)’ version of the BepiColombo Mercury Imaging X-ray Spectrometer (MIXS) instrument as described in Section 5. This corresponds to a time-area product of 250 m²s. As can be seen from Eq. A.3, the range error contribution due to the instrument is inversely proportional to the square root of the time-area product. Figure 3 gives a plot of the ecliptic longitude versus ecliptic latitude of each of the 35 pulsars to show the distribution of the pulsars on the sky.

3.2 Pulsar position uncertainties

The current status of pulsar position⁴ uncertainties is summarised in Table 1, column ‘Position error’, using the data from the ATNF catalogue [52], supplemented by an

¹ <http://simbad.u-strasbg.fr/simbad/>

² <http://www.atnf.csiro.au/people/pulsar/psrcat/>

³ 26 of the sources had XMM fluxes available; these were all utilised. The origins of the fluxes for the remaining sources, and the corresponding numbers of sources, were: Chandra – 1, ROSAT PSPC – 3, ROSAT HRI – 3, ASCA – 1, BeppoSax – 1. This ranking also indicates the preference order for selecting fluxes. Where ROSAT count rates were used they were converted to fluxes using a factor 1.24×10^{-11} (PSPC) and 3.66×10^{-11} (HRI) erg cm⁻² s⁻¹ / count/s (0.1–2.4 keV). To convert all ‘energy’ fluxes to photon cm⁻² s⁻¹, we have used a factor 4×10^8 ph/erg. We have not attempted to take account of the spectral shapes of individual sources.

⁴ ‘Position’ here means the astrometric location of the pulsar on the sky, in any ‘sky’ coordinate frame e.g. equatorial (RA, Dec), ecliptic, galactic.

Table 1 Pulsar parameters and range error values for 35 rotation-powered X-ray pulsars with detected pulses

Pulsar number	PSR	Type	Pulsar period (s)	Source total flux ($\text{ph cm}^{-2} \text{s}^{-1}$)	Flux reference	W50	Pulse power	Pulse reference	Range error – focussing $T_{\text{obs}}=5 \times 10^3$ s (km)	Range error – collimated $T_{\text{obs}}=5 \times 10^5$ s (km)	Position error (mas)	Rank - focussing	Rank - collimated	Rank – position error
80	B1937+21	ms	0.00155	1.4	BS	0.02	0.86	Ray+08; Graven+08; Cusumano+03	1.2	16	0.04	1	2	1
27	B0531+21	fd	0.03308	3200	RP	0.05	0.7	Ray+08; Graven+08	1.5	1.3	3.43	2	1	10
70	B1821-24	ms	0.00305	0.52	RP	0.03	0.98	Rois+98; Ray+08; Graven+08	5.9	110	6.01	3	5	11
24	J0218+4232	ms	0.00232	2.2	XM	0.11	0.73	Ray+08; Graven+08	9.1	100	31.12	4	3	15
23	J0205+6449	fd	0.06568	61	XM	0.03	0.2	Murray+02	45	110	714.49	5	4	29
26	J0437-4715	ms	0.00575	4.4	XM	0.3	0.37	Zavlin06	83	670	0.05	6	9	2
30	B0540-69	fd	0.05035	160	XM	0.45	0.67	Kaaret+01; Graven+08	96	160	69.07	7	6	18
41	J1012+5307	ms	0.00525	0.15	RH	0.1	0.77	Webb+04	110	2800	0.48	8	14	5
20	J0030+0451	ms	0.00486	1.0	XM	0.3	0.5	Becker+02	120	1800	21.35	9	11	14
55	B1509-58	fd	0.15065	180	XM	0.3	0.65	Rois+98; Graven+08	180	290	1216.4	10	7	32
86	J2124-3358	ms	0.00493	0.420	XM	0.4	0.56	Zavlin06	260	5300	0.79	11	17	8
69	J1811-1925	fd	0.06466	130	XM	0.3	0.2	Torii+99	300	520	1732.38	12	8	35
36	J0751+1807	ms	0.00347	0.13	XM	0.31	0.52	Webb+04	380	9900	7.23	13	20	13
58	J1617-5055	fd	0.06935	17	XM	0.34	0.5	Becker+02	410	1700	966.52	14	10	31
47	J1124-5916	fd	0.13531	8.2	XM	0.23	0.9	Hughes+03	440	2700	1259.94	15	13	33
28	J0537-6910	fd	0.01612	13	RP	0.1	0.02	Martin-Canillo+12	820	4100	1423.68	16	15	34
84	J2021+3651	fd	0.10372	4.5	XM	0.3	0.65	Hessels+04	830	6700	693.19	17	18	27
78	J1930+1852	fd	0.13685	11	XM	0.18	0.27	Camilo+02	1000	5300	826.04	18	16	30
44	B1055-52	fd	0.1971	6.1	XM	0.3	0.7	De Luca+05	1300	8800	209.51	19	19	22
35	J0737-3039	ms	0.02269	0.14	XM	0.25	0.7	Chatterjee+07	1400	3.50×10^4	0.35	20	26	3
88	J2229+6114	fd	0.05162	0.42	RH	0.2	0.5	Halpern+02	1500	3.10×10^4	710.84	21	24	28
38	B0833-45	fd	0.08932	470	XM	0.55	0.045		1800	2100	0.37	22	12	4

Table 1 (continued)

Pulsar number	PSR	Type	Pulsar period (s)	Source total flux (ph cm ⁻² s ⁻¹)	Flux reference	W50	Pulse power	Pulse reference	Range error – focussing T _{obs} =5x10 ³ s (km)	Range error – collimated T _{obs} =5x10 ⁵ s (km)	Position error (mas)	Rank - focussing	Rank - collimated	Rank – position error
53	J1420-6048	fd	0.06818	1.6	XM	0.2	0.2	Martin-Carillo+12; Becker+96	2100	2.70x10 ⁴	190.28	23	23	21
42	J1024-0719	ms	0.00516	0.036	RH	0.5	0.52	Zavlin06	2900	8.60x10 ⁴	0.67	24	29	6
33	J0633+1746	fd	0.23709	3.9	XM	0.35	0.5	De Luca+05	3100	2.70x10 ⁴	56.57	25	22	16
34	B0656+14	fd	0.38489	2.7	XM	0.3	0.24	De Luca+05	3300	1.20x10 ⁴	305.58	26	21	25
61	B1706-44	fd	0.10245	4.8	XM	0.54	0.22	McGowan+04	4200	3.30x10 ⁴	63.7	27	25	17
52	J1357-6429	fd	0.1661	0.82	XM	0.5	0.63	Zavlin07	6200	1.00x10 ⁵	163.37	28	30	20
29	J0538+2817	fd	0.14315	3.3	XM	0.5	0.18	McGowan+03	8200	7.50x10 ⁴	2.4	29	27	9
46	J1119-6127	fd	0.40774	0.33	XM	0.26	0.74	Gonzalez+05	1.30x10 ⁴	2.70x10 ⁵	246.05	30	33	23
40	B0950+08	fd	0.25306	0.34	XM	0.2	0.3	Becker+04	1.40x10 ⁴	3.10x10 ⁵	84.83	31	34	19
32	J0631+1036	fd	0.28777	0.84	AS	0.5	0.45	Torii+01	1.50x10 ⁴	2.40x10 ⁵	305.74	32	31	26
79	B1929+10	fd	0.22651	0.82	XM	0.5	0.32	Becker+06	1.70x10 ⁴	2.70x10 ⁵	6.67	33	32	12
73	J1846-0258	fd	0.32359	17	CX	0.35	0.055	Goethelf+00	1.80x10 ⁴	7.70x10 ⁴	249.88	34	28	24
31	B0628-28	fd	1.24441	0.16	XM	0.4	0.4	Becker+05	2.00x10 ⁵	5.00x10 ⁶	0.68	35	35	7

The range error values are given for focussing and collimated type instruments, and are calculated using the Wolter-I improved PSF focussing instrument described in Section 5 with T_{obs} = 5x10³ s and A_{eff} = 0.005 m². The rankings of pulsars according to the range errors of the two instrument types and the pulsar position error are also shown. The key to column headings is: ‘Pulsar number’ is an arbitrary reference number assigned by us; the pulsar name [7]; ‘Type’ is the class of XRP; ‘ms’ for MSP and ‘fd’ for field from Becker 2009; the pulsar period [7]; the ‘Source total flux’ is the time-averaged X-ray flux from various origins but mainly catalogues* from XMM, Chandra and ROSAT – from reference given in ‘Flux reference’ with key XM; XMM[78], CX: Chandra [61], RH/RP: ROSAT HRI/PSPC [65], BS: BeppoSax [58], AS: ASCA [73]; ‘W50’ is the X-ray Full Width Half Maximum (FWHM) pulse width as a fraction of pulse period derived from reference (given as abbreviated e.g. Becker+02 = Becker [3]) in ‘Pulse reference’; ‘Pulse power’ is the X-ray pulsed power as a fraction of the total time-averaged X-ray flux derived from reference given in ‘Pulse reference’; ‘Range error – focussing’ and ‘Range error – collimated’ are the range error contributions due to the instrument for the two types according to the analytic formula; ‘Position error’ is the pulsar sky (astrometric) position error derived from the ATNF catalogue [52] except for B0531+21 [47]; ‘Rank – focussing’, ‘Rank – collimated’ and ‘Rank – position error’ are the rankings of the pulsars according to the range errors of the two instrument types and the pulsar position error. * These catalogues were interrogated on-line via the Virtual Observatory (VO) interface to the CDS Vizier databases (<http://vizier.u-strasbg.fr/viz-bin/VizieR>)

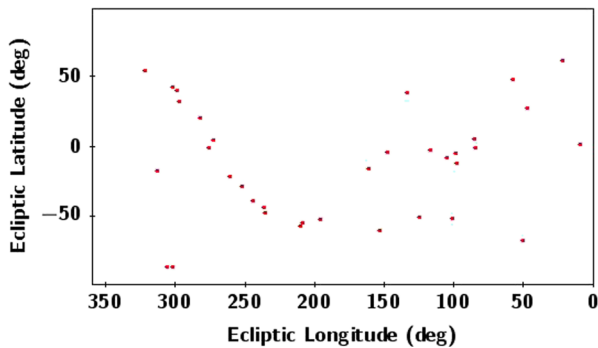


Fig. 3 Sky distribution in ecliptic coordinates of 35 X-ray pulsars relevant to this study, as listed in Table 1

improved value for the Crab pulsar [47]. Of the 35 pulsars listed, there are 8 with an overall position uncertainty of <1 mas, and 2 of these have a position uncertainty of <0.1 mas. Astrometry using X-ray, optical or ‘standard’ (e.g. relatively short baseline) radio measurements typically yields position uncertainties of ~ 0.1 – 1 arcsec. Higher precision astrometry for pulsars generally requires either pulse timing techniques or Very Long Baseline Interferometry (VLBI) (see e.g. [47, 48]). Long-term programmes to obtain high-precision pulsar positions and timing are in progress, driven by goals such as detection of gravitational-waves (see e.g. [38]). These programmes, and new instrumentation, e.g. the Square Kilometre Array (SKA) and its precursors, should lead to improved position uncertainties. It should also be noted that for high-precision positions, the effects of proper motion will need to be taken into account (see e.g. [48]) and possibly updated with contemporaneous measurements during XNAV operations.

3.3 Estimation of range error contributions due to the instrument

3.3.1 Using an analytic formula

A simple analytic formula can be used to estimate the spacecraft range measurement error based on the TOA measurement uncertainty alone by using the characteristics of each pulsar and the proposed instrumentation (e.g. [62]). This can be used for both focussing and collimated instrument types depending upon the input parameters and is largely independent of the specific method of TOA determination, such as cross-correlation, least-squares fitting or maximum likelihood. The formula and relevant details are given in Appendix A.

The above approach enables us to generate a ranking for the objects according to likely utility for XNAV, albeit with some simplifications and limitations. These include ignoring the detailed shape of the pulse profile and any variation with photon energy of the pulse profile and fractional pulsed emission; such energy dependence is evident in some cases, and differs in form between objects. In addition, some XRPCs such as the Crab and Vela pulsars lie within a region of significant extended X-ray emission due to the associated supernova remnant or a pulsar-wind nebula. We have attempted, where possible, to quote relatively low values for the pulsed fraction in such cases, recognising that a feasible XNAV instrument may not have sufficient spatial resolution to ‘reject’ the extended emission, which thus forms an additional background to the desired pulse signal. Figure 4

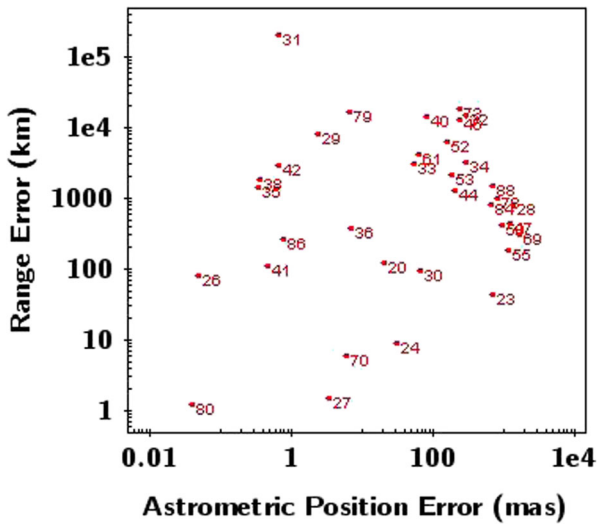


Fig. 4 Estimates of spacecraft range errors obtained using the analytic formula for 35 rotation-powered X-ray pulsars observed using the improved PSF focussing instrument described in Section 5 with $T_{\text{obs}} = 5 \times 10^3$ s and $A_{\text{eff}} = 0.005 \text{ m}^2$, versus pulsar astrometric position error. The most suitable sources for XNAV are thus towards the lower left of the plot. Each pulsar is identified by its pulsar number from Table 1, column 1; thus the 5 pulsars discussed in detail in this paper are numbers 26 (J0437-4715), 27 (B0531+21), 41 (J1012+5307), 70 (B1821-24) and 80 (B1937+21)

shows the range-error estimates for a focussing instrument, with $T_{\text{obs}} = 5 \times 10^3$ s, versus astrometric position error. The values are also listed in Table 1.

The scaling of the range errors (or TOA errors) for the different instrument types with observation time and effective area, and ranking of the pulsars according to these values, are relatively insensitive to the precise choice of background values. For example, assuming zero background does not change the set of 10 pulsars with the lowest range errors for the focussing instrument, though there are some changes in the ranking, and leads to a change in two cases near the lower boundary, for the collimated instrument.

3.3.2 Simulation of pulse profiles and comparison of range error estimates

We have performed simulations to examine in detail the effects of specific pulse profiles and instrument characteristics on the achievable TOA and range errors. The calculations used a model of the pulsed and unpulsed signal from the pulsar and the background fluxes, folded through the assumed instrument response and for a specified integration time, and with Poisson noise incorporated. Each simulated dataset was cross-correlated with the noiseless, model profile to determine a TOA error; the simulation was repeated typically 1000 times for each ‘observation’ in order to build-up a TOA-error distribution. An example, based on PSR B1937+21 as if viewed by our ‘baseline’ focussing instrument for an integration time of 50 ks, is shown in Fig. 5. The range error obtained from the simulations is computed as $W_{68}/2$, where W_{68} is the width of the distribution between the 16 % and 84 % percentiles (enclosing 68 % of the area of the distribution equivalent to the 1-sigma for a Gaussian distribution). This is a somewhat more ‘robust’

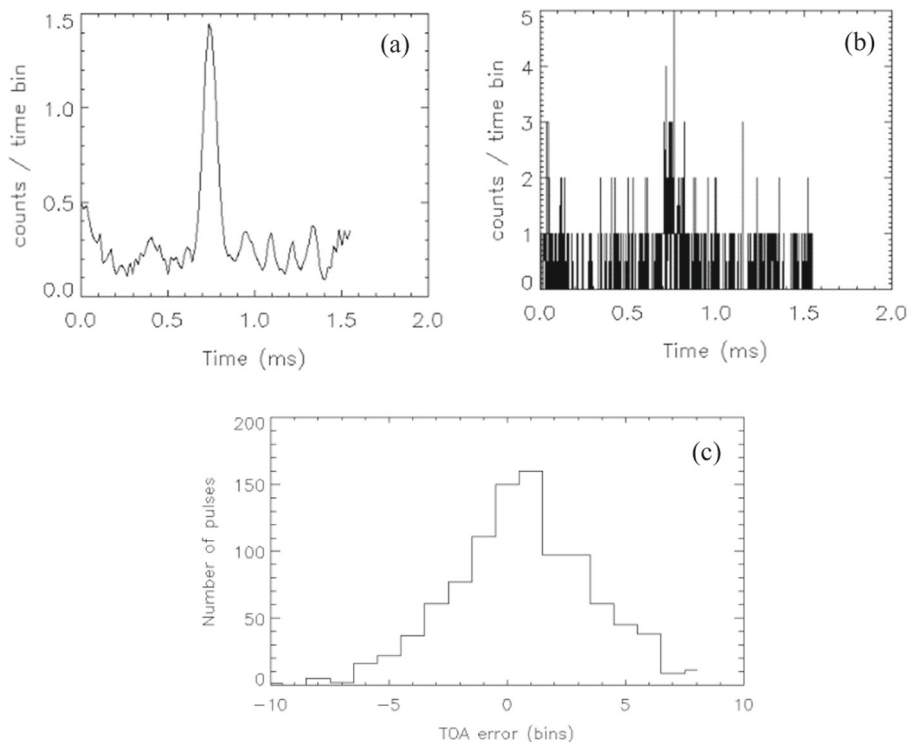


Fig. 5 An example of pulse TOA simulations for PSR B1937+21 using an integration time of 5×10^4 s with a BepiColombo-MIXS-type instrument. The plots show as follows: **a** the input (noiseless) model pulse profile based on data from the ROSSI X-ray Timing Explorer (RXTE), **b** the simulated pulse profile summed over the duration of the observation and **c** the TOA error distribution resulting from the simulated data where 1 bin $\approx 1.55 \mu\text{s}$ i.e. 10^{-3} of the pulse period

estimator than directly computing the standard deviation, given the ‘noise wings’ present for low SNR cases.

More accurate and complex formulae can be derived by detailed consideration of pulse shapes and statistics (e.g. [24, 36]); however the analytic formula described in Section 3.3.1 and Appendix A serves to highlight the main parametric dependencies. For a wide range of pulse-profile shapes and SNR, the values given by the formula and determined by the simulations for the five pulsars PSR B1937+21, B1821-24, J0437-4715, J1012+5307 and B0531+21 agree to within a factor of ~ 3 , and scale approximately with $1/\sqrt{T_{\text{obs}}}$ as expected and as can be seen in Table 2. A qualitative indication of the pulse shape in each case is also given in Table 2. We can thus have confidence in taking the analytic formula as an approximate guide, useful for indicating functional dependencies on the various parameters and for ranking the pulsars in terms of range error, whilst the simulations allow a more detailed evaluation of specific cases, for example the effects of low SNR or complex pulse profiles.

Comparison of our range-error estimates with some of those reported elsewhere [24, 34, 62], and bearing in mind possible differences in assumptions such as for pulsed and unpulsed fluxes and background fluxes, indicates general consistency.

4 Estimation of navigation and timing uncertainties from simulations

Two navigation strategies were outlined in Section 2; delta-correction using a single pulsar and absolute navigation using three or four pulsars. Appendix B describes the Monte Carlo approaches used to simulate the navigation errors achievable by each of these and some of the simulation outputs. These are used to identify the X-ray pulsars that would provide the lowest navigation uncertainties for each strategy. Here we present uncertainty budgets for PVT estimation using the best-performing pulsars identified for each navigation strategy. Finally, we summarise the results of the total uncertainties for PVT estimation in each case.

4.1 Navigation and timing uncertainty budgets

Simulations of errors are carried out using a similar approach to that in [34] (see Appendix B) using propagation of errors in the small perturbation case. These are partly based on the range errors due to the X-ray instrument for observation times, $T_{\text{obs}} = 5 \times 10^3$ and 5×10^4 s, obtained using the analytic formula (see Section 3.3.1). For improved uncertainty estimates, range errors obtained from simulations (see Section 3.3.2) instead of the analytic formula have been used for the five pulsars PSR B1937+21, B1821-24, J0437-4715, J1012+5307 and B0531+21. In the case of the latter pulsar, the errors are obtained by appropriate scaling of the values given in Table 2.

For the results presented in this section, and as described in Appendix B, a latency period of 3 months is assumed in the cases of four pulsars. This refers to the interval between two timing model updates during a period of autonomous navigation and allows us to take account of the range error contributed by pulsar timing model error. In the case of the Crab pulsar, a much shorter period of order 3 days has been assumed.

Table 2 Comparison of range-error estimates from the analytic formula and simulations

PSR	Pulse Period (ms)	Pulse fractional width, FWHM	Pulse shape	Observation time, T_{obs} (ks)	Range error (km), from formula	Range error (km), from simulation
B1937+21	1.55	0.02	sharp, single	5	1.2	4.4
				50	0.38	1.2
B1821-24	3.05	0.03	sharp, double	5	5.9	10.0
				50	1.9	2.8
J0437-4715	5.75	0.3	broad, asymmetric single	5	83.0	67.0
				50	26.0	16.0
J1012+5307	5.25	0.1	sharp, single	5	110.0	41.0
				50	35.0	23.0
B0531+21 (Crab)	33.08	0.05	sharp, double	0.01	34.0	55.0
				0.1	10.5	15.0

The results are based on the Wolter-I design with improved PSF described in Section 5

As the errors used as input to the simulations are representative of 1-sigma uncertainties, the outputs of the simulations are equivalent to 1-sigma uncertainties. These should be taken as indicative values because they vary depending on the exact values of the input data used for each pulsar.

The outputs are expressed in the form of uncertainty budgets for the best performing and other selected pulsars identified for each navigation strategy. These apply specifically to a spacecraft located in the ecliptic plane at a distance of 30 AU from the SSB in the direction of zero degrees ecliptic longitude and latitude, corresponding to ecliptic coordinates given by $x=30$ AU, $y=0$ AU and $z=0$ AU. The velocity vector is taken to be of magnitude 30 km s^{-1} in the direction of zero degrees ecliptic longitude and latitude. However, in most cases the position uncertainty budgets are found to be reasonably representative of spacecraft ranges of 30 AU in other directions from the SSB within the ecliptic plane. The largest variation is found in the single pulsar case of using the Crab pulsar. Here, for example, the position uncertainty budget can be lower by about one order of magnitude in the direction of 90° ecliptic longitude and zero degrees latitude, corresponding to ecliptic coordinates given by $x=0$ AU, $y=30$ AU and $z=0$ AU. The simulations do not take account of any knowledge about the trajectory of the spacecraft and the use of a Kalman filter.

The navigation and timing uncertainty budgets comprise mainly two components (see Eqs B.2 to B.10 in Appendix B). The first is largely due to the TOA measurement uncertainties arising from the instrument, with a contribution also from the pulsar timing model uncertainty. The second is due to the pulsar position uncertainties on the sky, which leads to the spacecraft position and clock time-offset uncertainties increasing linearly with range from the SSB, whilst the velocity and time-drift rate uncertainties increase linearly with velocity.

Table 1 demonstrates that a higher performance is expected from a focussing instrument and consequently the results presented in this section are based on using this type of instrument. The effective area is based on existing technology, i.e. the BepiColombo MIXS-T instrument [29] which has an effective area of 0.005 m^2 , as described in Section 5; we assume an improved PSF, as also described in Section 5.

Table 3 presents the uncertainty budgets with the two components for the three pulsar-set PSR B1937+21, B1821-24 and J0437-4715 which gives the lowest position uncertainty for $T_{\text{obs}}=5 \times 10^4$ s and for PSR B1937+21, B0531+21 and J0437-4715 which gives the lowest uncertainty whilst also including the Crab pulsar. These are given for observation times, T_{obs} , of 5×10^3 and 5×10^4 s. For the latter pulsar-set with $T_{\text{obs}}=5 \times 10^4$ s, the position uncertainty budget is lower by a factor of ~ 2 at ecliptic coordinates given by $x=0$ AU, $y=30$ AU and $z=0$ AU. It is found that although the former pulsar set gives the lowest position uncertainty of any three pulsar set for $T_{\text{obs}}=5 \times 10^4$ s, PSRs B1937+21, B1821-24 and J1012+5307 give the lowest uncertainty for $T_{\text{obs}}=5 \times 10^3$ s corresponding to 80 km. The contribution due to pulsar position uncertainties in this case is 25 km. A consequence of using the simulated range errors is that the optimum pulsar set depends on the observation time. Table 4 presents the relevant uncertainty budgets when using four pulsars and Table 5 for a single pulsar in the cases of PSR B1937+21 and the Crab pulsar.

The simulations are applicable to scenarios related to interplanetary navigation, which accounts for the majority of deep space missions. The approaches described can be used to evaluate uncertainties for any velocity vector, including one inclined to

Table 3 Spacecraft position and velocity uncertainty budgets for absolute navigation at ecliptic coordinates $x=30$ AU, $y=0$ AU and $z=0$ AU using the three-pulsar set giving the lowest position uncertainties (for $T_{\text{obs}} = 5 \times 10^4$ s) and for the three pulsar-set giving the lowest uncertainties whilst also including the Crab pulsar, PSR B0531+21

Uncertainty Source	PSR B1937+21, B1821-24, J0437-4715				PSR B1937+21, B0531+21, J0437-4715			
	Position Uncertainty Contribution (km)		Velocity Uncertainty Contribution (ms^{-1})		Position Uncertainty Contribution (km)		Velocity Uncertainty Contribution (ms^{-1})	
	$T_{\text{obs}} = 5 \times 10^4$ s	$T_{\text{obs}} = 5 \times 10^3$ s	$T_{\text{obs}} = 5 \times 10^4$ s	$T_{\text{obs}} = 5 \times 10^3$ s	$T_{\text{obs}} = 5 \times 10^4$ s	$T_{\text{obs}} = 5 \times 10^3$ s	$T_{\text{obs}} = 5 \times 10^4$ s	$T_{\text{obs}} = 5 \times 10^3$ s
Instrument and timing model	30	120	0.6	25	30	110	0.6	20
Pulsar position	20	20	0.1×10^{-3}	0.1×10^{-3}	90	90	0.6×10^{-3}	0.6×10^{-3}
Total uncertainty	35	120	0.6	25	100	140	0.6	20

the plane of the ecliptic, and any spacecraft location within the Solar System and to some extent beyond.

4.2 Summary of navigation and timing uncertainties

The PVT uncertainties derived in this section are summarised in Table 6. The spacecraft positioning uncertainty component due to the pulsar position uncertainty can be calculated for other ranges using the uncertainty budgets given. To do this the ratio of the required range to 30 AU is multiplied by the given value of this component at 30 AU. In this way, results for a spacecraft at a distance of 1 AU from the SSB are also shown in Table 6 for comparison.

It should be noted that the performance results given at 1 AU in Table 6 are for the best-performing pulsar-sets determined at ecliptic coordinates given by $x=30$ AU, $y=0$ AU and $z=0$ AU. Other pulsar sets may have similar or marginally lower

Table 4 Spacecraft position, clock time-offset, velocity uncertainty and time drift rate uncertainty budgets for absolute navigation at ecliptic coordinates $x=30$ AU, $y=0$ AU and $z=0$ AU using the four pulsar-set giving the lowest position uncertainties

Uncertainty Source	PSR B1937+21, B1821-24, J1012+5307 and J0437-4715							
	Position Uncertainty Contribution (km)		Time-Offset Uncertainty Contribution (s)		Velocity Uncertainty Contribution (ms^{-1})		Time Drift Rate Uncertainty Contribution (ss^{-1})	
	$T_{\text{obs}} = 5 \times 10^4$ s	$T_{\text{obs}} = 5 \times 10^3$ s	$T_{\text{obs}} = 5 \times 10^4$ s	$T_{\text{obs}} = 5 \times 10^3$ s	$T_{\text{obs}} = 5 \times 10^4$ s	$T_{\text{obs}} = 5 \times 10^3$ s	$T_{\text{obs}} = 5 \times 10^4$ s	$T_{\text{obs}} = 5 \times 10^3$ s
Instrument and timing model	30	80	40×10^{-6}	100×10^{-6}	0.6	15	1×10^{-9}	20×10^{-9}
Pulsar position	20	20	10×10^{-6}	10×10^{-6}	0.1×10^{-3}	0.1×10^{-3}	6×10^{-14}	6×10^{-14}
Total uncertainty	35	80	40×10^{-6}	100×10^{-6}	0.6	15	1×10^{-9}	20×10^{-9}

Table 5 Spacecraft position and velocity uncertainty budgets for the delta-correction method at ecliptic coordinates $x=30$ AU, $y=0$ AU and $z=0$ AU using a single pulsar with PSR B1937+21 and B0531+21

Uncertainty Source	PSR B1937+21				PSR B0531+21			
	Position Uncertainty		Velocity Uncertainty		Position Uncertainty		Velocity Uncertainty	
	Contribution (km)		Contribution (ms^{-1})		Contribution (km)		Contribution (ms^{-1})	
	$T_{\text{obs}} = 5 \times 10^4$ s	$T_{\text{obs}} = 5 \times 10^3$ s	$T_{\text{obs}} = 5 \times 10^4$ s	$T_{\text{obs}} = 5 \times 10^3$ s	$T_{\text{obs}} = 5 \times 10^4$ s	$T_{\text{obs}} = 5 \times 10^3$ s	$T_{\text{obs}} = 5 \times 10^4$ s	$T_{\text{obs}} = 5 \times 10^3$ s
Instrument and timing model	1.4	4.6	0.03	1	3.7	5.5	0.07	1
Pulsar position	0.7	0.7	6×10^{-6}	6×10^{-6}	70	70	500×10^{-6}	500×10^{-6}
Total uncertainty	1.5	4.7	0.03	1	70	70	0.07	1

uncertainties at 1 AU from the SSB. Furthermore, the analysis here uses pulsar position uncertainties currently available in the literature. These will improve in future by different amounts depending on the pulsar, as new measurements become available.

5 Available and future X-Ray technology

XNAV requires high signal-to-noise timing observations of one or more pulsars to derive a spacecraft position estimate. There is a trade-off between the ability to generate high signal-to-noise observations of this type and the requirement of a positioning system to be deployable as a spacecraft subsystem, where mass, volume and power consumption are tightly constrained. XNAV requires a time resolution of $<1 \mu\text{s}$ (a significant performance improvement is possible if 100 ns is achievable) and a high collecting area, the value of which depends upon whether the instrument is imaging or not. Ideally the system would be able to simultaneously observe up to three or four pulsars which are widely separated on the sky. In this section, we first describe the required characteristics of instrumentation for an XNAV system. We then discuss some of the design and development challenges that need to be overcome. Finally, we discuss the technology trade-offs and optimisations that need to be considered regarding instrument performance.

5.1 Observing pulsars for X-ray astronomy

X-ray instruments used in astrophysics, in general, use single photon-counting detectors; hence are well suited for use in timing studies [28]. Literature on instrumentation for high time-resolution pulsar astrophysics is dominated by collimated instruments (e.g. [42]). However, in recent studies of the XNAV concept [8] imaging instrumentation is proposed to allow the use of more capable solid-state focal plane devices which offer higher positioning accuracy due to reduced background and hence higher signal-to-noise.

Table 6 A summary of the PVT uncertainties for a spacecraft located in the ecliptic plane at a distance of 30 AU and 1 AU from the SSB in the direction of zero degrees ecliptic longitude and latitude

Navigation strategy & pulsars	Parameter	30 AU		1 AU	
		$T_{\text{obs}} = 5 \times 10^4 \text{ s}$	$T_{\text{obs}} = 5 \times 10^3 \text{ s}$	$T_{\text{obs}} = 5 \times 10^4 \text{ s}$	$T_{\text{obs}} = 5 \times 10^3 \text{ s}$
(i) Absolute navigation using three pulsars PSR B1937+21, B1821-24, J0437-4715	Position	35 km	120 km	30 km	120 km
	Velocity	0.6 ms^{-1}	25 ms^{-1}	0.6 ms^{-1}	25 ms^{-1}
(ii) Absolute navigation using three pulsars PSR B1937+21, B1821-24, J1012+5307	Position	50 km	80 km	45 km	80 km
	Velocity	0.9 ms^{-1}	15 ms^{-1}	0.9 ms^{-1}	15 ms^{-1}
(iii) Absolute navigation using three pulsars PSR B1937+21, B0531+21, J0437-4715	Position	100 km	140 km	30 km	110 km
	Velocity	0.6 ms^{-1}	20 ms^{-1}	0.6 ms^{-1}	20 ms^{-1}
(iv) Absolute navigation using four pulsars PSR B1937+21, B1821-24, J1012+5307, J0437-4715	Position	35 km	80 km	30 km	80 km
	Clock time-offset	$40 \times 10^{-6} \text{ s}$	$100 \times 10^{-6} \text{ s}$	$40 \times 10^{-6} \text{ s}$	$100 \times 10^{-6} \text{ s}$
	Velocity	0.6 ms^{-1}	15 ms^{-1}	0.6 ms^{-1}	15 ms^{-1}
	Clock time-drift rate	$1 \times 10^{-9} \text{ ss}^{-1}$	$20 \times 10^{-9} \text{ ss}^{-1}$	$1 \times 10^{-9} \text{ ss}^{-1}$	$20 \times 10^{-9} \text{ ss}^{-1}$
(v) Delta-correction using a single pulsar with PSR B1937+21	Position (in direction of pulsar)	1.5 km	4.7 km	1.4 km	4.6 km
	Velocity (in direction of pulsar)	0.03 ms^{-1}	1 ms^{-1}	0.03 ms^{-1}	1 ms^{-1}
(vi) Delta-correction using a single pulsar with PSR B0531+21	Position (in direction of pulsar)	70 km	70 km	4.5 km	6 km
	Velocity (in direction of pulsar)	0.07 ms^{-1}	1 ms^{-1}	0.07 ms^{-1}	1 ms^{-1}

These may be achievable with a focussing instrument with an effective area of 0.005 m^2 and are representative of 1-sigma

Orbiting observatories dedicated to high time resolution astronomy are designed to fulfil multiple scientific goals and as such are not optimised specifically for the XNAV principle. They are generally dedicated payloads (or at least a dominant instrument) on a low earth orbit mission. For a practical XNAV system to be developed, instrumentation must be designed to meet the following requirements:

- i. large collecting area to minimise statistical noise in observations of faint sources;
- ii. high timing accuracy - typically $<1 \mu\text{s}$ time stamping uncertainty;
- iii. low background noise from internal and external sources (such as the detector intrinsic background, particle induced signals, cosmic rays and the diffuse X-ray background);
- iv. Engineering constraints (low mass, volume, power consumption).

But crucially, the system must also be implementable as a realistic spacecraft subsystem, hence a particular emphasis on requirement iv in what follows.

5.2 The advantage of imaging

The primary scientific justification for true X-ray imaging, rather than scanning with a collimated instrument over a specific field of view is to reduce background. In a true imaging system, the signal collecting area is greater than the collecting area relevant for background noise. In such a system, the relevant area for (non-sky⁵) background collection is equal to the size of the optic PSF, rather than the whole area of the detector (as would be the case for a collimated instrument). The effective collecting area for the signal is governed principally by the aperture of the optic and its focal length.⁶ Combining these effects, the signal-to-noise ratio of an imaging system is improved by the “*imaging advantage*” (I) defined as:

$$I = \sqrt{\frac{A_{eff}}{A_{BG}}},$$

where A_{eff} is the effective collecting area of the optic and A_{BG} , the detection cell size in the detector plane (governed by the optic PSF). This assumes that the sky background (diffuse X-ray background and confusion limited point sources) is negligible, which may not be true depending on the characteristics of the pulsar. In such a case, the background contribution from the sky must be accounted for when assessing the improvement in signal-to-noise as a result of imaging.

Of course, there are additional benefits of imaging which range from engineering parameters (smaller detectors: less particle shielding, simpler thermal control, simplified focal plane design) to scientific observation advantages such as a reduction in “sky background” from diffuse X-ray emission and unresolvable point sources on the sky. The only significant disadvantage of an imaging system is the need to design a sufficiently accurate pointing mechanism capable of steering an ~ 1 m focal length telescope to acquire the pulsar of interest.

A collimated XNAV system would require a minimum focal plane area $\sim 10^3$ cm². Assuming a large-area collimated silicon detector were to be used, the cooling of the detectors and shielding them from high energy particles would be difficult to achieve as a small, optimised, XNAV subsystem. Also, the overall system complexity would be considerable, particularly when the requirement to perform photon time-tagging with microsecond uncertainty over the whole detector area is considered. While a much larger system has been studied for the Large Observatory for X-ray Timing (LOFT) mission [27] as the dominant instrument of a large satellite [82], it is difficult to foresee a time when this level of complexity could be integrated into a spacecraft navigation subsystem, even though the LOFT hardware is well-suited to the XNAV principle.

⁵ Note that the sky background is proportional to the optic effective area as well as the relevant focal plane area.

⁶ The maximum useful aperture is driven by the critical angle for X-ray reflection, hence the dependence on focal length.

Recent developments in low-mass optics (e.g. [29, 81]) have enabled the design of compact imagers, requiring greatly reduced spacecraft resources compared to established X-ray optics technologies. This technological advancement offers the possibility of implementing a true imaging X-ray telescope in a resource envelope commensurate with a sub-system on a deep space vehicle. The first example of such an instrument to be deployed in deep space will be the Mercury Imaging X-ray Spectrometer (MIXS) [29], one of 11 instruments on the ESA/JAXA BepiColombo mission to Mercury [9]. The telescope, MIXS-T could be considered a “pathfinder” for XNAV technology as it is designed to very similar engineering constraints. Figure 6 shows the key components of the MIXS-T instrument.

5.3 Design and development challenges for an XNAV instrument

Below we discuss the principal design and development challenges that must be addressed in order to realise an operational XNAV instrument.

5.3.1 Observing strategy

As described in Section 2.2.2, the most capable XNAV system would incorporate simultaneous observations of a minimum of three or four pulsars. However, the complexity of a multiple field-of-view X-ray instrument, with separate telescopes that are independently steerable would be high, making it challenging to implement. It is much more reasonable to envisage a single pointed instrument being deployed on a deep space mission. Similarly, ideal XNAV observations would be long, uninterrupted stares towards targets of interest. Although there are no intrinsic limits on the observation duration set by the detector system, practical limitations will come from specific mission scenarios. For instance, the instrument will have pointing constraints relating to solar-system objects (typically; the Sun, nearby planets and moons) that will limit the available sky and the observation duration. X-ray instruments have a solar avoidance angle typically $\sim 30\text{--}40^\circ$, so the fraction of the sky that is not visible at any given time may be significant.

5.3.2 Optics

MicroChannel-Plate (MCP) optics are the key enabling technology for low-mass (<10 kg) imaging X-ray instruments (e.g. [29, 54]). MIXS uses a radially packed array of microscopic square pores to simulate the mirror shells of a more traditional Wolter-I

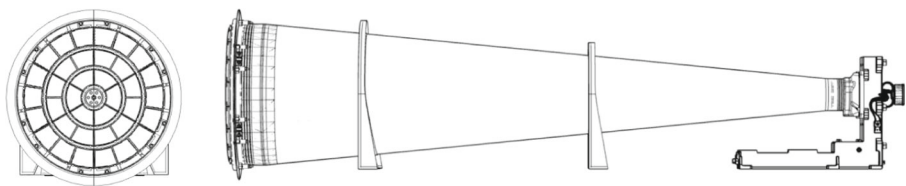


Fig. 6 Diagram showing the key components of the BepiColombo MIXS-T imaging Wolter-I telescope comprising a microchannel plate optic (left), a telescope tube assembly and a focal plane assembly containing a DEPFET active pixel sensor detector (right)

telescope and meets similar resource constraints as an XNAV system. The optics themselves are made of lead-glass septal walls, the result of a manufacturing process which etches millions of microscopic pores from the glass. For MCP optics, these channels are square in cross-section and can be coated with high atomic number material to increase the reflectivity of the channel walls, improving the collecting power of the telescope. The total mass of the MIXS instrument is only ~ 10 kg including the electronics boxes, mechanics and a collimated instrument, MIXS-C [29], which is of no direct relevance to XNAV. The telescope has a focal length of 1 m and offers an effective area of ~ 0.005 m² with a high performance silicon DEPFET active pixel sensor detector. The detector is optimised for spectroscopy and provides almost Fano-limited energy resolution [51]. Hence, it does not operate at the time resolution required for XNAV, but could be replaced by a suitable detector, as discussed below.

Significant simplification and optimisation of the MIXS design is possible for XNAV. Either a narrow field lobster-eye telescope [1] or a cylindrical microchannel plate approximation to the Kirkpatrick-Baez (KB) geometry [45] offers a simpler optical design with higher spatial resolution (and hence lower background) than the current ~ 7 – 10 arcminutes. Proof-of-principal experiments with a partial prototype of the KB system have demonstrated ~ 3 arcminutes FWHM. A programme of work to demonstrate the limiting performance of a lobster-eye optic is underway at the University of Leicester and Photonis France, SAS. It is realistic to expect an optic with large collecting area and improved imaging resolution to emerge from a dedicated research and development programme.

Note that the simulations of XNAV performance reported here are based on MIXS-like hardware, but assume an improved PSF of 3.5 arcminutes FWHM. It should be noted that while existing hardware can already meet the major goals of XNAV, improvements in the optic presented here lead directly to smaller range errors (due to better rejection of background by a higher quality optic). The performance improvement varies for different pulsars based on their brightness. A better optic is insignificant for the Crab, but offers improvements up to ~ 50 % for the weaker sources such as PSR J1012+5307.

5.3.3 Detectors

Considering available detector technologies, the optimum existing device for XNAV is an extremely fast, single pixel, Silicon Drift Detector (SDD), examples of which are available from AMPTEK Inc. and PN Detector GmbH. For example, AMPTEK's super-fast SDD offers excellent energy resolution, close to the fundamental Fano limit, if operated with long peaking times, or, if operated with very fast peaking times (~ 0.2 μ s), the energy resolution is degraded, but the time resolution is improved. As energy resolution is not a fundamental driver for XNAV – it only allows rejection of background based on photon energy – this degraded energy resolution is not a significant driver and fast shaping time is preferred.

The absolute timing accuracy of the device is not only a function of the peaking time. As the X-ray can strike anywhere in the active detector volume, and the charge generated by the X-ray interaction is drifted to a readout node, the time-delay variation caused by the drifting of charge will increase the error in measuring the absolute arrival time of the photon. To match the expected performance of the optic and detector a

diode of diameter 2.5 mm is required and the quantum efficiency should be maximised in the range $\sim 0.5\text{--}8$ keV. For such a large pixel, it is unlikely to be able to achieve a time resolution of better than ~ 0.5 μs due to the physics of drifting charge to the readout. By using a pixelated device with small pixels, the drift time is reduced and higher limiting time resolution is possible; such devices are under development for applications in high flux X-ray sources such as free electron lasers with time resolution in the low hundreds of ns (e.g. [60]), a development that could be important for future XNAV studies.

5.3.4 On-board clock and timing

The requirements for maintaining on-board timing precision are stringent, but not outside the scope of existing technology. For instance, the clocks on-board the Galileo satellites [23] would offer precision considerably greater than needed for an XNAV system during single observations of up to a few days. The complication in provision of a timing reference is in maintaining high accuracy absolute time relative to terrestrial time scales such as TAI (Temps Atomique International) over the lifetime of a deep space mission. This would be required when positioning in the direction of a single pulsar or in order to reduce the numbers of pulsars to be observed from four to three for three-dimensional positioning. Pulse TOA measurements need to be obtained relative to terrestrial time scales, ideally to better than 300 ns, without timing drift becoming a significant error source. In the next decade, it is possible that a clock with sufficient stability may be demonstrated in space. For example, NASA is currently developing a deep space mercury ion-trap atomic clock [72]. Without such a clock, it would be necessary to employ a time transfer link to Earth using the DSN to periodically calibrate the on-board clock relative to, for example, TAI. If in the future an instrument with a significantly improved TOA measurement error was to be employed, a clock with commensurately lower uncertainty would be required. For example, a space optical clock similar to those currently under development (e.g. [67]), could be of benefit to a long-duration advanced space experiment.

5.4 Technology trade-offs and optimisation

Detailed system design is outside the scope of this paper. However, it is possible to parameterise the performance of the instrument in terms of its focal length (hence mass) and key XNAV figures of merit such as the signal-to-noise ratio and the range error contribution due to the instrument. The focal length influences these performance parameters via its relationship to focal-plane scale and effective area [1].

In Fig. 7 (right panel) this approach is used to show that the range error decreases with increasing instrument focal length (and hence collecting area), showing that instruments with a focal length of 25 cm may be useful for the Crab pulsar and PSR B1937+21, but for a navigation system to be generally applicable to fainter pulsars, a longer focal length (e.g. the baseline 1 m described below) is required. Figure 7 (left) shows that, except for the Crab pulsar, the signal to noise ratio per unit mass increases for longer focal lengths, implying that a larger (more capable) telescope provides a more mass efficient solution with longer focal lengths. Hence, a larger telescope is preferable to an approach reliant on multiple, co-pointing telescopes to increase the

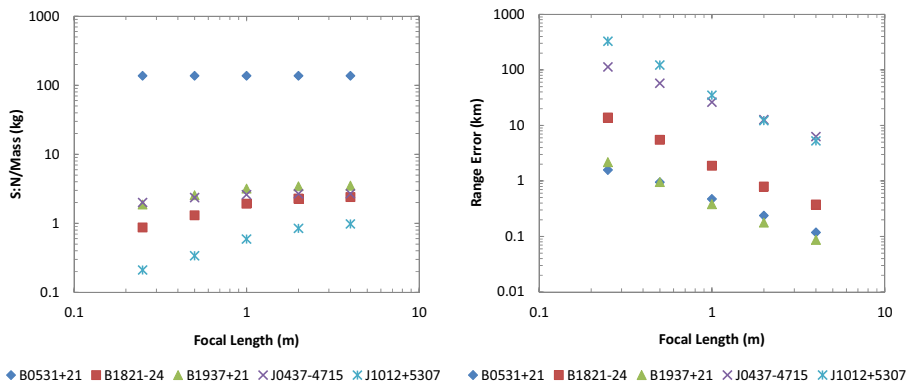


Fig. 7 Left- the Signal-to-Noise ratio (S:N) per unit mass versus focal length for 5 pulsars assuming an observation of 5×10^4 s. Right- the range error obtained using the analytic formula (see Section 3.3.1) as a function of focal length for 5 pulsars. The different order of the pulsars in the two panels is a result of the relative importance of signal strength, the pulse width and pulse period of the various pulsars

collecting area (assuming the dominant consideration for spacecraft resource planning is mass). The optimum, practically realisable system for XNAV is likely to be based on the light weight optics described here, specifically, a single (steerable) KB optic coupled to an SDD detector.

The properties and predicted performance of such a telescope are described in Table 7. In assessing the spacecraft resources required for this proposed device a number of assumptions are made. It is assumed that a (currently) low maturity instrument based on a KB design can be achieved for a similar mass as the MIXS-T Wolter I design. To cover the risk of this low maturity, a small margin (0.7 kg) is added to the predicted optic mass. The 6.4 kg detector and housing includes a conservative estimate of 5.5 kg for a radiation shield to protect the detectors from solar protons and other ionizing radiation. The DPU mass is estimated based on SSTL's OBC750 LEO unit.

Table 7 also provides an estimate of the power consumption for the device which includes; the DPU (10 W), detector and front-end electronics (0.25 W), analogue electronics (2 W), PSU efficiency (70 %). The power estimate is based on the experience of MIXS and excludes thermal control (assumed to be provided by a spacecraft radiator).

6 Discussion

As described in Curkendall and Border 2013, a single one of the antennas used in NASA's DSN can be used to carry out two-way ranging to a spacecraft to measure its distance along the line-of-sight to the Earth extremely precisely to an uncertainty of a few metres. Furthermore, pairs of antennas can also be used at a time for very long baseline interferometry measurements referred to as Delta-Differential One-Way Ranging (Delta-DOR). By doing this, the DSN can currently be used to obtain tracking uncertainties approaching 1 nrad, equivalent to 150 m and 4.5 km in the plane of the sky for spacecraft distances of 1 AU and 30 AU from Earth respectively. This means that uncertainties of 150 m are possible at an Earth-Mars distance of 1 AU. At a range

Table 7 Summary of the characteristics of an imaging XNAV system (excluding thermal control and telescope pointing mechanisms) based on an instrument similar to MIXS-T and a more optimised KB optic

Parameter	MIXS-T	KB Optic	Units
Optic Performance			
Optic effective area	50	80	cm ² @ 1keV
Focal plane scale	3.44	3.44	arcmin/mm
Mass estimate			
Optic mass	1.8	~2.5	kg
Detector/housing	6.4	6.4	kg
DPU	1.5	1.5	kg
PSU	1	1	kg
Harness and misc.	1	1	kg
TOTAL	11.7	12.4	kg
Volume estimate			
Telescope:	250x250x1000	260x260x1000	mm ³
DPU:	320x170x55	320x170x55	
PSU:	320x170x55	320x170x55	
Detector Parameters			
Type	APD/SDD	APD/SDD	
Time resolution	1 (0.3 goal)	1 (0.3 goal)	μs
Cooling required	-20	-20	°C
Detector active area	0.049	0.049	cm ²
Quantum efficiency	>90	>90	%
Power consumption estimate	15.9	15.9	W

of 30 AU and for $T_{\text{obs}} = 5 \times 10^4$ s, three-dimensional XNAV positioning uncertainties for an improved PSF version of the BepiColombo-MIXS instrument given in Table 6 are generally ~one order of magnitude greater than those described above for the DSN, although with the potential for being somewhat lower in the direction of PSR B1937+21. However, with the exception of the cases when the Crab pulsar is used, these uncertainties could be achieved without the need to communicate with Earth to update the pulsar's timing model for up to 3 months. In the case of Delta-DOR for the ESTRACK network, the tracking uncertainties are currently 6 to 15 nrad [41], although there are ongoing studies with the aim of improving these to 1 nrad. The XNAV positioning uncertainties are generally of the same order at a range of 30 AU, although more than an order of magnitude lower in the direction of PSR B1937+21. A key advantage for XNAV is that, unlike the use of the ESTRACK or DSN systems for navigation, it could allow a greater level of spacecraft autonomy because it requires significantly less communication with Earth-based systems.

With $T_{\text{obs}} = 5 \times 10^4$ s, the effects of the first component due to instrument and timing model uncertainties and the second component due to pulsar position uncertainties are of a similar order of tens of kilometres for each of the three and four pulsar cases at a distance of 30 AU from the SSB. For the single and three-pulsar cases involving the

Crab pulsar, the effect of pulsar position uncertainty can be the larger component by far for some spacecraft locations. For $T_{\text{obs}} > 1 \times 10^5$ s (~ 1 day), the effect of pulsar position uncertainties would start to dominate in the other cases. Consequently, this component may be the limiting factor in determining spacecraft position. However, if the latency period of the timing model for each pulsar, apart from for the Crab pulsar, was to become on the order of years then the effect of timing model uncertainties would begin to dominate. In the case of the Crab pulsar, this would apply if the latency period was on the order of months. If pulsar position uncertainties reduce in future, the spacecraft position uncertainties would also reduce. However, in the case of the velocity uncertainties, these are always dominated by the instrument and timing model uncertainties for the above T_{obs} values.

From Eqs B.2, B.5 and B.8 (see Appendix B), it can be seen that for the XNAV positioning error, the component due to pulsar position error increases with spacecraft range from the SSB. From Table 6, it can be seen that the spacecraft position uncertainties are generally of the same order at ranges of 1 and 30 AU for a given T_{obs} value of 5×10^4 or 5×10^3 s. In the single pulsar case of the Crab, the position uncertainties at 1 AU are much lower due to the relatively high pulsar position uncertainty of this pulsar. Apart from for this particular case, the spacecraft position uncertainties at 1 AU are heavily dominated by the instrument and timing model uncertainties.

Out of the pulsars considered, the three-pulsar set PSR B1937+21, B1821-24 and J0437-4715 is found to show the lowest spacecraft position uncertainty at 30 AU for $T_{\text{obs}} = 5 \times 10^4$ s and one of the lowest at 1 AU. It also shows one of the lowest velocity uncertainties. The two position uncertainty components, the total uncertainty and how these vary with distance from the SSB are shown in Fig. 8. For a typical distance of Mars from the SSB, 1.5 AU, the total uncertainty is ~ 30 km after observing each pulsar for 5×10^4 s. The set PSR B1937+21, B1821-24 and J1012+5307 would show a similar performance for up to 3 months. A disadvantage of using the set PSR B1937+21, B0531+21 and J0437-4715 would be the need for much higher timing model updates, for example daily, to be transmitted to the spacecraft using the ESTRACK or the DSN systems due to the much higher timing noise and rate of glitches [50] exhibited by the Crab pulsar. The two former three-pulsar sets would require much less frequent timing model updates and allow a higher level of spacecraft autonomy.

Apart from for the cases when the Crab pulsar is used, it is found that the uncertainties would not in general be expected to increase significantly above those given in Table 6 for several months without a timing model update i.e. 6 months. However, some caution is required as there is a small probability of a glitch [50] occurring in one of the pulsars and this may result in the accuracy of the timing model very rapidly degrading. No glitches have so far been observed in any MSP apart from PSR B1821-24 for which a micro-glitch has once been observed [15]. This glitch was two orders of magnitude smaller than any ever observed before. If this pulsar exhibited a similar sized glitch again during a 3 month period where there was no communication with Earth to update the timing model, the spacecraft position uncertainties for the three pulsar set PSR B1937+21, B1821-24, J0437-4715 would be greater by up to ~ 10 km. This would correspond to a total uncertainty of up to ~ 40 km for an Earth-Mars trajectory, compared to ~ 30 km in the more likely case of a glitch not having occurred. To mitigate the impact of a glitch in PSR B1821-24, observations could be periodically complemented by

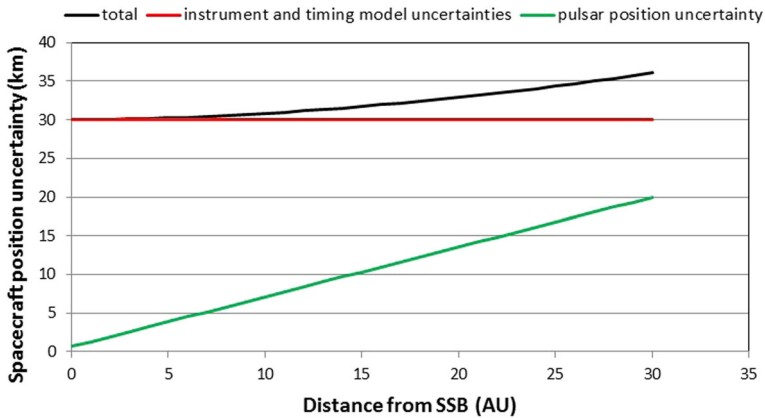


Fig. 8 The variation of the spacecraft position uncertainty and its main components with distance from the SSB for the three-pulsar set PSR B1937+21, B1821-24 and J0437-4715 and for $T_{\text{obs}} = 5 \times 10^4$ s. The uncertainty components shown are firstly due to the X-ray instrument and timing model uncertainties and secondly due to the pulsar position uncertainty

observations of a three pulsar set that excludes the above pulsar for cross-verification and replaced by these if necessary.

In the case of using a single pulsar, uncertainties of ~ 5 and ~ 1.5 km may be achieved in the direction of PSR B1937+21 with $T_{\text{obs}} = 5 \times 10^3$ s (~ 1 h) and 5×10^4 s (~ 10 h) respectively for a distance of up to 30 AU from the SSB. Current systems would require up to 8 h for providing a spacecraft with position information in this scenario. The positioning uncertainty of the DSN and ESTRACK systems in the plane of the sky are 4.5 and 45 km respectively for a spacecraft at 30 AU. XNAV has the potential to provide more accurate position information along the direction of PSR B1937+21. Depending on the geometry of the particular scenario, this could then be combined with the information from the DSN to enable reduced position uncertainties in the plane of the sky [34].

By assuming that the motion of the spacecraft can be adequately accounted for, the XNAV uncertainties would reduce by \sqrt{N} where N is the number of observations. However, in practice this will be limited by the errors in the trajectory models including due to the effects of tertiary bodies in the Solar System and solar radiation pressure over long time intervals [21].

As described in Sections 2 and 4, an XNAV system capable of simultaneous observations of a minimum of three or four pulsars for absolute navigation would provide the greatest capability. However, as described in Section 5.3.1, the implementation of an instrument allowing adequate measurement uncertainties on a spacecraft would be a significant challenge. It may be more realistic to consider an instrument making sequential observations of multiple pulsars. For this scenario, the observation times, T_{obs} , given in Section 4 and Appendix B for absolute navigation using three and four pulsars would need to be multiplied by three and four respectively.

It is found that similar position and velocity uncertainties can be achieved using three pulsars together with an accurate atomic clock instead of using four pulsars. Having to observe only three pulsars may mean a simpler instrument design is possible. Another advantage is that, obviously, if a single telescope instrument is used (see Section 5.3.1) it would take less time to sequentially observe three pulsars than four

pulsars. The clock would need to provide suitable traceability to terrestrial time scales over the lifetime of the mission. Alternatively, this could be achieved by regular measurements with the DSN, although this would reduce spacecraft autonomy.

Pulsar position geometry is also a factor in navigation performance. As described in Appendix B, Geometric Dilution of Precision (GDOP) provides a measure of the geometry of the distribution of pulsars in the sky. Ideally the pulsars should be as widely distributed in the sky as possible.

It should be emphasised that the uncertainties derived in this paper correspond to those for the Wolter-I ‘improved PSF’ focussing instrument as described in Section 5 with the aim of achieving a realistic spacecraft subsystem. These will differ from those of other X-ray instruments.

The instrumentation needs of an XNAV system have been shown in Section 5 to be compatible with available technologies. However, significant improvements in performance and increased spacecraft autonomy are expected from the adoption of new technology in the next decade. Potential technological improvements exist in all three of the major subsystems considered here as follows. Improving the optic reduces background noise and offers lower positioning uncertainty. Improving the detector system e.g. to generate very high time resolution would lead to better absolute timing of a pulsar and allow improved estimates of a pulse TOA. A time resolution requirement of $<1 \mu\text{s}$ may be met with existing technology, but the significant performance improvement offered by a 100 ns uncertainty may be achieved in the next decade. Finally, improvements in the stability of atomic clocks for space applications is also expected and this would offer the possibility of reducing the number of pulsars that need to be observed to allow autonomous navigation.

Radio observations of pulsars could in principle be used in combination with or as an alternative to X-ray. However, the potential requirement of large radio antennas [8] means that a practical solution would need to be identified to meet the resource constraints of a deep space mission.

7 Conclusions

In this paper we have investigated the feasibility of deep-space navigation using X-ray pulsars. Simulations show that the pulsar PSR B1937+21 has potential to allow spacecraft positioning uncertainties of ~ 2 and ~ 5 km in the direction of the pulsar after observation times of 10 and 1 h respectively, for distances up to 30 AU. The advantage of this technique is that, unlike existing systems such as NASA’s DSN and ESA’s ESTRACK networks, this could be achieved autonomously on-board the spacecraft, using an X-ray instrument of effective area $\sim 50 \text{ cm}^2$ and a high performance atomic clock. A practical X-ray telescope may, for example, be an ‘improved PSF’ version of the BepiColombo-MIXS instrument. For a manned mission to Mars, where an XNAV system could provide valuable redundancy, observations of the three pulsars PSR B1937+21, B1821-24 and J0437-4715, would enable a three-dimensional positioning uncertainty of ~ 30 km for up to 3 months without having to contact Earth-based systems. This would require a total observation time of 10 h if using an instrument with multiple telescopes or 2 days with a single telescope. The uncertainty may be lower using longer observations, although at greater ranges such as 30 AU the present

limiting factor is often due to uncertainties in the pulsar positions on the sky. If these were to significantly reduce in future, the navigation uncertainties would also reduce in such cases.

X-ray instrumentation suitable for use in an operational XNAV subsystem must be designed to require only modest resources, especially in terms of size/volume, mass and power. In addition to our Wolter-1 (BepiColombo) concept which involves a focussing optic, the possible options for future developments in terms of simpler and lower-cost Kirkpatrick-Baez or Lobster optics have been examined. Significant scope exists to derive an optic from one of these simpler designs with better performance than currently possible. Detectors with the necessary count rate capacity, time resolution and quantum efficiency are commercially available but electronic time tagging of X-ray photons to the required accuracy needs further study. Absolute time uncertainty on-board a spacecraft is one of the limiting factors for spacecraft autonomy. This could be improved by use of a sufficiently accurate atomic clock.

Acknowledgments The work reported in this paper is based on that performed primarily under European Space Agency Contract No. 4000105938/12/NL/KML. We thank Pietro Giordano and Jaron Samson for their interest and encouragement in the study. Microchannel plate optics have been developed by Photonis SAS, Brive France, in collaboration with the University of Leicester funded by ESA contracts. We thank Paul Houghton and Jon Sykes (University of Leicester) for providing the BepiColombo MIXS-T diagram in Fig. 6. We are grateful to John Davis at the National Physical Laboratory for constructive comments during preparation of the manuscript.

Appendix

Appendix A: estimation of range error contribution due to the instrument, using an analytic formula

From the basic statistics of a frequency distribution it follows that (e.g. [62, 69]; see also [48], Sect. 8.1.2):

$$\sigma_L \sim c\sigma_{\text{TOA}} \sim Kc\text{HWHM}_{\text{pulse}}/\text{SNR} \quad (\text{A.1})$$

where σ_L is the spacecraft range error; c is the speed of light; σ_{TOA} is the pulse TOA error; $\text{HWHM}_{\text{pulse}}$ is the pulse ‘characteristic width’ expressed as Half Width at Half Maximum (HWHM); SNR is the Signal-to-Noise Ratio; K is a dimensionless factor which embodies the detailed shape of the profile representing a weighting of the SNR across the profile with a typical value of between 1 and 0.5. σ_L and σ_{TOA} can then be expressed in terms of the characteristics of the pulsar and the observing instrument, as detailed below.

SNR can be expressed as:

$$\text{SNR} = C_p / (C_p + C_s + C_b)^{0.5} \quad (\text{A.2})$$

where: C_p =net pulsed counts summed over the pulse profile; C_s =unpulsed source counts; C_b =counts from all other background contributions within the ‘source

beam’ = $C_{bX} + C_{bN}$; C_{bX} = detected counts due to “diffuse” X-ray background (XRB) from the sky; C_{bN} = detected counts due to cosmic-ray background (CRB) and other sources of internal detector noise. We can then derive

$$\sigma_L = c \sigma_{TOA} = c \sigma_\phi P \approx 0.5 K c W_{50} P (C_p + C_s + C_b)^{0.5} / C_p$$

$$\sigma_L \approx 0.5 K c W_{50} P \left[(A_{\text{eff}} T_{\text{obs}} f_{\text{psf}} F_{\text{total}})^{0.5} X_p \right]^{-1} \left[1 + (f_{\text{psf}} F_{\text{total}})^{-1} (F_{bX} \Omega_{\text{eff}} + F_{bN} A_{\text{det}} / A_{\text{eff}}) \right]^{0.5} \quad (\text{A.3})$$

where P is the pulse period (s), W_{50} is the pulse profile Full Width Half Maximum [FWHM] as a fraction of the pulse period, X_p is the fraction of the power in the pulse compared to the total time-averaged flux, A_{eff} is the instrument effective area (m^2) averaged over the instrument energy band, A_{det} is the source-detection area (m^2) equal to the full detector area for the collimated case and the source-detection cell area for the focussing case, Ω_{eff} is the source-detection solid angle (sr) equal to the collimator FOV for the collimated case, T_{obs} is the observation duration (s), f_{psf} is the fraction of PSF within the source-detection area, F_{total} is the total X-ray flux from the pulsar, F_{bX} is the diffuse X-ray background flux from the sky ($\text{ph cm}^{-2} \text{s}^{-1} \text{sr}^{-1}$) and F_{bN} is the flux due to the cosmic-ray background and other sources of internal detector noise ($\text{ct cm}^{-2} \text{s}^{-1}$). This expression for the range error comprises a term (i) $0.5 K \dots X_p \dots^{-1}$ representing the pulsar properties and a dimensionless multiplicative term (ii) $[1 + \dots F_{bN} A_{\text{det}} / A_{\text{eff}}]^{0.5}$ representing the background components. Note that the above formulation relates to the Poisson noise only, and does not include, for example, any pulse jitter noise or the effect of pulsar position uncertainty.

Appendix B: Method of estimating navigation and timing uncertainties from simulations

B.1 Absolute Navigation

As described in Section 2.2.2, absolute navigation requires three or more pulsars. The approach described in Graven et al. [34] for deriving spacecraft position error when using three pulsars can be used as a starting point. Here the main errors are due to the pulse TOA measurement and the sky positions of the pulsars. The geometry of pulsars in the sky is also an important factor. It is assumed that there is sufficiently accurate traceability to terrestrial time scales on-board the spacecraft. Using an ecliptic coordinate system in cartesian form with its origin at the SSB, the spacecraft x , y and z position coordinates are then given by

$$\begin{bmatrix} x \\ y \\ z \end{bmatrix} = \begin{bmatrix} x_1 & y_1 & z_1 \\ x_2 & y_2 & z_2 \\ x_3 & y_3 & z_3 \end{bmatrix}^{-1} \begin{bmatrix} \frac{cP_1}{2\pi} \varphi_1 \\ \frac{cP_2}{2\pi} \varphi_2 \\ \frac{cP_3}{2\pi} \varphi_3 \end{bmatrix} \quad (\text{B.1})$$

where φ_i , $[x_i, y_i, z_i]$ and P_i are the measured pulse phase in radians, the unit vector and the period of the i th pulsar respectively. Using the approach given in Graven et al. [34],

which involves propagation of errors in the small perturbation case, the error in the spacecraft position is given by

$$\begin{bmatrix} \delta x \\ \delta y \\ \delta z \end{bmatrix} = \begin{bmatrix} x_1 & y_1 & z_1 \\ x_2 & y_2 & z_2 \\ x_3 & y_3 & z_3 \end{bmatrix}^{-1} \begin{bmatrix} \frac{cP_1}{2\pi} \Delta\varphi_1 \\ \frac{cP_2}{2\pi} \Delta\varphi_2 \\ \frac{cP_3}{2\pi} \Delta\varphi_3 \end{bmatrix} - \begin{bmatrix} x_1 & y_1 & z_1 \\ x_2 & y_2 & z_2 \\ x_3 & y_3 & z_3 \end{bmatrix}^{-1} \begin{bmatrix} \Delta x_1 & \Delta y_1 & \Delta z_1 \\ \Delta x_2 & \Delta y_2 & \Delta z_2 \\ \Delta x_3 & \Delta y_3 & \Delta z_3 \end{bmatrix} \begin{bmatrix} x \\ y \\ z \end{bmatrix} \tag{B.2}$$

where $\Delta\varphi_i$ and $[\Delta x_i, \Delta y_i, \Delta z_i]$ are the errors in the phase measurement and the unit vector of the i th pulsar respectively. The position of each pulsar $[x_i, y_i, z_i]$ is obtained from its ecliptic coordinates and $[\Delta x_i, \Delta y_i, \Delta z_i]$ from the errors in the coordinates. The error in the measured phase $\Delta\varphi_i$ is mainly a result of the phase measurement error due to the X-ray instrument. As described later, we also include in $\Delta\varphi_i$ a contribution for the pulsar timing model error allowing also for an estimated level of timing noise. $cP_i\Delta\varphi_i/2\pi$ is equivalent to the overall range error taken for the i th pulsar. We assume any system level timing errors to be small compared to the error sources described above. The errors in ecliptic coordinates are derived using the errors in right ascension and declination.

The approach given in Bernhardt et al. [10] for determining spacecraft position error using three pulsars does not appear to consider the effect of pulsar position errors. This may be a suitable approximation for inner Solar System locations where the effect is relatively small, but its impact becomes increasingly important with range from the SSB [34]. Consequently, the approach used in this paper (Eq. B.2) would lead to a higher spacecraft position error than that of Bernhardt et al. [10] if the same properties of the pulsars and instrument were used, although the difference may only be significant at larger ranges.

We extend the above approach of Graven et al. [34] to the error in spacecraft velocity. It can be shown that if the velocity components of the spacecraft are given by \dot{x}, \dot{y} and \dot{z} , the velocity error components $\delta\dot{x}, \delta\dot{y}$ and $\delta\dot{z}$ can be determined using

$$\begin{bmatrix} \delta\dot{x} \\ \delta\dot{y} \\ \delta\dot{z} \end{bmatrix} = \begin{bmatrix} x_1 & y_1 & z_1 \\ x_2 & y_2 & z_2 \\ x_3 & y_3 & z_3 \end{bmatrix}^{-1} \begin{bmatrix} \Delta d_1 \\ \Delta d_2 \\ \Delta d_3 \end{bmatrix} - \begin{bmatrix} x_1 & y_1 & z_1 \\ x_2 & y_2 & z_2 \\ x_3 & y_3 & z_3 \end{bmatrix}^{-1} \begin{bmatrix} \Delta x_1 & \Delta y_1 & \Delta z_1 \\ \Delta x_2 & \Delta y_2 & \Delta z_2 \\ \Delta x_3 & \Delta y_3 & \Delta z_3 \end{bmatrix} \begin{bmatrix} \dot{x} \\ \dot{y} \\ \dot{z} \end{bmatrix} \tag{B.3}$$

where Δd_i is the error in d_i given by

$$d_i = \frac{c(f_i - f_{mi})}{f_{mi}} \tag{B.4}$$

where f_i is the measured pulse frequency of the i th pulsar, and f_{mi} is the expected pulse frequency in the reference frame of the SSB, as given by the pulsar’s timing model.

In the case where there is a significant spacecraft clock time-offset from terrestrial time scales, a minimum of four pulsars is required in order to also estimate this offset. We extend the above approach to the four pulsar case where the position and time errors are given by

$$\begin{bmatrix} \delta x \\ \delta y \\ \delta z \\ -c\delta t_c \end{bmatrix} = \begin{bmatrix} x_1 & y_1 & z_1 & 1 \\ x_2 & y_2 & z_2 & 1 \\ x_3 & y_3 & z_3 & 1 \\ x_4 & y_4 & z_4 & 1 \end{bmatrix}^{-1} \begin{bmatrix} \frac{cP_1}{2\pi} \Delta\varphi_1 \\ \frac{cP_2}{2\pi} \Delta\varphi_2 \\ \frac{cP_3}{2\pi} \Delta\varphi_3 \\ \frac{cP_4}{2\pi} \Delta\varphi_4 \end{bmatrix} - \begin{bmatrix} x_1 & y_1 & z_1 & 1 \\ x_2 & y_2 & z_2 & 1 \\ x_3 & y_3 & z_3 & 1 \\ x_4 & y_4 & z_4 & 1 \end{bmatrix}^{-1} \begin{bmatrix} \Delta x_1 & \Delta y_1 & \Delta z_1 \\ \Delta x_2 & \Delta y_2 & \Delta z_2 \\ \Delta x_3 & \Delta y_3 & \Delta z_3 \\ \Delta x_4 & \Delta y_4 & \Delta z_4 \end{bmatrix} \begin{bmatrix} x \\ y \\ z \end{bmatrix} \quad (\text{B.5})$$

where δt_c is the error in the clock time-offset. This is analogous to pseudorange errors determined in GPS [44]. In this case, the velocity error components $\delta\dot{x}$, $\delta\dot{y}$ and $\delta\dot{z}$ can be determined using

$$\begin{bmatrix} \delta\dot{x} \\ \delta\dot{y} \\ \delta\dot{z} \\ -c\delta\dot{t}_c \end{bmatrix} = \begin{bmatrix} x_1 & y_1 & z_1 & 1 \\ x_2 & y_2 & z_2 & 1 \\ x_3 & y_3 & z_3 & 1 \\ x_4 & y_4 & z_4 & 1 \end{bmatrix}^{-1} \begin{bmatrix} \Delta d_1 \\ \Delta d_2 \\ \Delta d_3 \\ \Delta d_4 \end{bmatrix} - \begin{bmatrix} x_1 & y_1 & z_1 & 1 \\ x_2 & y_2 & z_2 & 1 \\ x_3 & y_3 & z_3 & 1 \\ x_4 & y_4 & z_4 & 1 \end{bmatrix}^{-1} \begin{bmatrix} \Delta x_1 & \Delta y_1 & \Delta z_1 \\ \Delta x_2 & \Delta y_2 & \Delta z_2 \\ \Delta x_3 & \Delta y_3 & \Delta z_3 \\ \Delta x_4 & \Delta y_4 & \Delta z_4 \end{bmatrix} \begin{bmatrix} \dot{x} \\ \dot{y} \\ \dot{z} \end{bmatrix}, \quad (\text{B.6})$$

where $\delta\dot{t}_c$ is the error in the drift rate of the clock.

Equation B.2 enables simulation of errors for position, using errors in pulse phase measurements and pulsar positions for three pulsars. Similarly Eq. B.5 enables simulation of errors for position and time, using the errors for four pulsars. Phase measurement errors of the instrument ($=\sigma_{\text{TOA},i}/P_i$) due to combined source- and background-noise contributions for both focussing and collimated instruments have generally been estimated analytically as described in Section 3.3.1 and Appendix A. However, for the five pulsars PSR B1937+21, B1821-24, J1012+5307, J0437-4715 and B0531+21 these have been obtained using simulations of pulse profiles as described in Section 3.3.2. Position and time errors have been simulated by conducting Monte Carlo simulations using the errors in the pulse phase measurements and pulsar positions. Due to the large numbers of three- and four-pulsar combinations that are possible using 35 pulsars, we have reduced the amount of computation by simulating errors for a smaller sample of 10 pulsars with the lowest values of range error contribution due to the instrument as given in Table 1. Furthermore, as can be seen from Table 1, a focussing instrument enables significantly lower range errors than a collimator. Consequently, we present the results of simulations considering a focussing instrument for the 10 pulsars with the lowest range errors using such an instrument.

The pulsar positions, pulsar frequencies and their errors have been taken from the X-ray pulsar catalogue described in Section 3. Random errors, according to a Gaussian distribution with 1 sigma given by the uncertainty in the relevant parameter, have been generated for each pulsar as inputs to Eq. B.2 in order to determine the δx , δy and δz error components. This is repeated 100 times in order that the distribution of output

errors in each case can be used to estimate a representative value for the 1-sigma position uncertainty. A similar process is used to derive 1-sigma uncertainties in all other PVT estimation cases. The instrument effective area is based on existing technology, i.e. the BepiColombo MIXS-T instrument [29] which has an effective area of 0.005 m^2 , as described in Section 5.

The ATNF pulsar catalogue [52] gives a value for the uncertainty in the Crab pulsar timing model frequency of 10^{-7} Hz . This has been derived using a long data-set of several years [49] and is affected at least by timing noise in the rotation of the pulsar. We consider that this value may be pessimistic and have used a value of 10^{-10} Hz that we believe should be realistic using a shorter span of Crab pulsar data.

Table 8 shows the six three-pulsar sets that give the lowest position uncertainties for a spacecraft located at a distance of 30 AU from the SSB at ecliptic coordinates given by $x=30 \text{ AU}$, $y=0 \text{ AU}$ and $z=0 \text{ AU}$. The position uncertainty given in each case is obtained from the square-root of the sum of the squares of the uncertainties along each of the x -, y - and z -axes of the ecliptic coordinate system which form an error ellipsoid. The observation time for each pulsar is taken to be $5 \times 10^4 \text{ s}$, resulting in a time-area product of $250 \text{ m}^2\text{s}$. It can be seen that the pulsar-set given by B1937+21, B1821-24 and J0437-4715 provides the lowest uncertainties. Pulsar position geometry is also a factor in navigation performance. A measure of the geometry in this case is the Position Dilution of Precision (PDOP) [44, 59]. A lower PDOP value corresponds to a better geometry. The value of this is also shown for each pulsar-set in Table 8. Similarly, Table 9 shows the five four-pulsar-sets that give the lowest combined position and clock time-offset uncertainties for a spacecraft located at the same point in the Solar System as above. The best set corresponds to B1937+21, B1821-24, J0437-4715 and J1012+53. The pulsar position geometry factor in this case, for position and time estimation, is called the Geometric Dilution of Precision (GDOP) and is also given in Table 9.

For some pulsars, a representative value has also been taken for the pulsar timing model error. This was the case for the pulsars PSR B1937+21, B1821-24, J1012+5307, J0437-4715 and B0531+21. For the first four pulsars we have assumed a latency period of 3 months between the last TOA used to derive the timing model and the XNAV observation epoch on-board the spacecraft. With the exception of the Crab pulsar, the timing model error, allowing also for an estimate of timing noise, is expected

Table 8 Position uncertainties for absolute navigation in the ecliptic plane using three pulsars and an observation time of $5 \times 10^4 \text{ s}$ for each pulsar

Pulsar-set	PDOP	Position uncertainty (km)
B1937+21, B1821-24, J0437-4715	2.9	35
B1937+21, B1821-24, J1012+5307	2.8	50
B1821-24, J0437-4715, J0030+0451	1.8	80
B1937+21, J1012+5307, J0030+0451	1.9	85
J1012+5307, J0437-4715, J0030+0451	2.1	90
B1937+21, B 0531+21, J0437-4715	2.6	95

These apply to a spacecraft with ecliptic coordinates $x=30 \text{ AU}$, $y=0 \text{ AU}$ and $z=0 \text{ AU}$. The six pulsar-sets with the lowest uncertainties are shown together with the PDOP in each case.

Table 9 Position and clock time-offset uncertainties for absolute navigation in the ecliptic plane using four pulsars and an observation time of 5×10^4 s for each pulsar

Pulsar-set	GDOP	Time-offset uncertainty (s)	Position uncertainty (km)
B1937+21, B1821-24, J1012+5307, J0437-4715	2.6	0.00004	35
B1937+21, B1821-24, J1012+5307, J0030+0451	2.5	0.0001	65
B1821-24, J1012+5307, J0437-4715, J0030+0451	1.7	0.00005	75
B1937+21, 0531+21, B1821-24, J1012+5307	2.5	0.0001	85
B1937+21, J1012+5307, J0437-4715, J0030+0451	2.2	0.00005	100

These apply to a spacecraft with ecliptic coordinates $x=30$ AU, $y=0$ AU and $z=0$ AU. The five pulsar-sets with the lowest position uncertainties are shown. Values of GDOP are also shown for each pulsar-set

to be highest as a fraction of the TOA measurement error (obtained using simulations of pulse profiles as in Section 3.3.2) for PSR B1821-24. Based on the data presented in Cognard et al. [17], we have taken a first order representative value of this to be $5 \mu\text{s}$, equivalent to $\sim 50\%$ of the TOA measurement error for an observation time of 5×10^4 s. For PSR B1937+21, J1012+5307 and J0437-4715 this is taken to be of order 20%, 20% and 1% respectively based on the data given in Cognard et al. [16], Lange et al. [46] and Verbiest et al. [75]. In the case of the Crab pulsar, the timing model error is likely to be at least tens of microseconds for a latency period which could conceivably be 1 month or less due to timing models for this pulsar being published more frequently compared to those of other pulsars [49]. We have assumed the error to be $10 \mu\text{s}$ which corresponds to a latency period of order 3 days. For cases where this is below $\sim 200 \mu\text{s}$, the dominant error source would be that due to the pulsar's position error.

The first five rows of Table 10 show the five three-pulsar-sets that offer the lowest velocity uncertainties for a time-area product of $250 \text{ m}^2\text{s}$ based on the 10 pulsars assessed in detail. In this case the spacecraft is considered as having a velocity of 30 km s^{-1} relative to the SSB in the direction of zero ecliptic longitude and latitude. The

Table 10 Velocity uncertainties for absolute navigation in the ecliptic plane using three pulsars and an observation time of 5×10^4 s for each pulsar

Pulsar-set	Velocity uncertainty (ms^{-1})
B1937+21, B1821-24, J0218+4232	0.4
B1821-24, J0218+4232, J0437-4715	0.5
B1937+21, J0218+4232, J0437-4715	0.6
B0531+21, B J0218+4232, J0437-4715	0.6
B1937+21, B 0531+21, J0437-4715	0.6
B1937+21, B1821-24, J0437-4715	0.6

The six pulsar-sets with the lowest uncertainties are shown based on the 10 pulsars assessed.

five pulsar-sets do not include the pulsar-set identified with the lowest position uncertainty in Table 8. The velocity uncertainty for this is shown for comparison in the bottom row of Table 10. Similarly, Table 11 shows four-pulsar-sets with their velocity uncertainties.

B.2 Delta-correction measurement using a single pulsar

This is the simplest strategy [34, 69] as described in Section 2.2.1 and represented in Fig. 1. The position-offset $\underline{\Delta r}$ can be defined as follows

$$\underline{\Delta r} = \underline{r} - \tilde{\underline{r}}, \tag{B.7}$$

where \underline{r} is the actual position of the spacecraft and $\tilde{\underline{r}}$ is the estimated position. Using a similar approach to that used for absolute navigation (see Section B.1), the error in the position-offset in the direction of the pulsar is given by

$$\hat{\underline{n}} \cdot \delta \underline{\Delta r} = \frac{cP}{2\pi} \Delta\varphi - d\hat{\underline{n}} \cdot \underline{r} \tag{B.8}$$

where $d\hat{\underline{n}}$ is the error in the unit vector to the pulsar, $\Delta\varphi$ is the error in the pulse phase measurement due to the X-ray instrument and pulsar timing model. Equation B.8 has been used to simulate uncertainties in spacecraft position-offset. The simulation assumes a spacecraft position in the ecliptic plane with a range of 30 AU from the SSB at ecliptic coordinates given by $x = 30$ AU, $y = 0$ AU and $z = 0$ AU. Table 12 shows the six pulsars that give the lowest position uncertainties in the direction of the pulsar with a focussing instrument and a time-area product of 250 m²s. PSR B1937+21 yielded the lowest uncertainty.

Table 11 Velocity and clock time-drift rate uncertainties for absolute navigation in the ecliptic plane using four pulsars and an observation time of 5×10^4 s for each pulsar

Pulsar-set	Time-drift rate uncertainty (ss ⁻¹)	Velocity uncertainty (ms ⁻¹)
B1937+21, B0531+21, B1821-24, J0218+4232	0.2x10 ⁻⁹	0.4
B1937+21, B0531+21, J0218+4232, J0437-4715	0.3x10 ⁻⁹	0.4
B0531+21, B1821-24, J0218+4232, J0437-4715 ,	0.3x10 ⁻⁹	0.5
B1937+21, B1821-24, J0218+4232, J1012+5307	0.6x10 ⁻⁹	0.6
B1937+21, B1821-24, J1012+5307, J0437-4715	0.8x10 ⁻⁹	0.6
B1937+21, B0531+21, B1821-24, J1012+5307	0.3x10 ⁻⁹	0.7

The six pulsar-sets with the lowest velocity uncertainties are shown based on the 10 pulsars assessed. The last row shows the uncertainty for the only pulsar set given in Table 9 which includes the Crab pulsar. This corresponds to the pulsar set with the 8th lowest uncertainty

Table 12 Position uncertainties in the ecliptic plane using the delta-correction method with a single pulsar and an observation time of 5×10^4 s

PSR	Position uncertainty in the direction of the pulsar (km)
B1937+21	1.5
B1821-24	12
J0437-4715	16
J1012+5307	30
J0030+0451	65
B0531+21	70

These apply to a spacecraft with ecliptic coordinates $x=30$ AU, $y=0$ AU and $z=0$ AU. The six pulsars with the lowest uncertainties are shown

Similarly to above, the velocity-offset of the spacecraft, $\underline{\Delta v}$, can be defined as

$$\underline{\Delta v} = \underline{v} - \underline{\tilde{v}} \quad (\text{B.9})$$

where, \underline{v} , is the actual velocity of the spacecraft and $\underline{\tilde{v}}$ is the estimated velocity. The error in the velocity-offset, $\delta \underline{\Delta v}$, in the direction to the pulsar is given by

$$\hat{n} \cdot \delta \underline{\Delta v} = \Delta d - d \hat{n} \cdot \underline{v} \quad (\text{B.10})$$

where $d \hat{n}$ is as described above and Δd is the error in d , as defined in Eq. B.4, and given by the error in the pulse frequency measurement due to the X-ray instrument and the frequency error of the pulsar timing model. We assume any system level timing errors to be small compared to the error sources described above. Table 13 shows the seven pulsars that give the lowest velocity uncertainties in the direction of the pulsar with a focussing instrument and a time-area product of $250 \text{ m}^2 \text{ s}$. As in the previous cases, the spacecraft is considered as having a velocity of 30 kms^{-1} relative to the SSB in the direction of zero degrees ecliptic longitude and latitude. In this case, PSR B1937+21 again yielded the lowest uncertainty.

Table 13 Velocity uncertainties in the ecliptic plane using the delta-correction method with a single pulsar and an observation time of 5×10^4 s

PSR	Velocity uncertainty in the direction of the pulsar (ms^{-1})	Timing model frequency error (Hz)
B1937+21	0.03	1.3×10^{-12}
J0218+4232	0.06	3×10^{-10}
B1821-24	0.07	6×10^{-10}
B0531+21	0.07	10^{-10}
J0205+6449	0.30	2×10^{-11}
J0437-4715	0.35	3×10^{-12}
J1012+5307	0.60	4×10^{-12}

The seven pulsars with the lowest uncertainties are shown based on the 10 pulsars assessed. The timing model frequency error used is also given in each case

Open Access This article is distributed under the terms of the Creative Commons Attribution 4.0 International License (<http://creativecommons.org/licenses/by/4.0/>), which permits unrestricted use, distribution, and reproduction in any medium, provided you give appropriate credit to the original author(s) and the source, provide a link to the Creative Commons license, and indicate if changes were made.

References

1. Angel, J.R.P.: Lobster eyes as X-ray telescopes. *Astrophys. J.* **233**, 364–373 (1979)
2. Becker, W., Truemper, J.: ROSAT observations of gamma-ray pulsars: vela, PSR 1706–44 and PSR 1951 + 32. *Astron. Astrophys.* **120C**, 69 (1996)
3. Becker, W., Aschenbach, B.: X-ray Observations of Neutron Stars and Pulsars: First Results from XMM-Newton, in *Neutron Stars, Pulsars and Supernova Remnants*, eds. W. Becker, H. Lesch, J. Truemper, MPE-Report 278, p. 64 (astro-ph/0208466) (2002)
4. Becker, W., Weisskopf, M.C., Tennant, A.F., Jessner, A., Dyks, J., Harding, A.K., Zhang, S.N.: Revealing the X-Ray emission processes of Old rotation-powered pulsars: XMM-newton observations of PSR B0950 + 08, PSR B0823 + 26, and PSR J2043 + 2740. *Astrophys. J.* **615**, 908 (2004)
5. Becker, W., Jessner, A., Kramer, M., Testa, V., Howaldt, C.: A multiwavelength study of PSR B0628-28: the first overluminous rotation-powered pulsar? *Astrophys. J.* **633**, 367 (2005)
6. Becker, W., Kramer, M., Jessner, A., Taam, R.E., Jia, J.J., Cheng, K.S., Mignani, R., Pellizzoni, A., De Luca, A., Slowikowska, A., Caraveo, P.A.: A multiwavelength study of the pulsar PSR B1929 + 10 and its X-Ray trail. *Astrophys. J.* **645**, 1421 (2006)
7. Becker, W.: X-ray emission from pulsars and neutron stars. In: Becker, W. (ed.) *Neutron stars and pulsars*, pp. 91–140. Springer, ASSL (2009)
8. Becker, W., Bernhardt, M. G., Jessner, A.: *Autonomous Spacecraft Navigation with Pulsars*. (2013) Accessed 3 June (2013)
9. Benkhoff, J., van Casteren, J., Hayakawa, H., Fujimoto, M., Laakso, H., Novara, M., Ferri, P., Middleton, H.R., Ziethe, R.: BepiColombo—Comprehensive exploration of Mercury: Mission overview and science goals. *Planet. Space Sci.* **58**, 2–20 (2010)
10. Bernhardt, M. G., Prinz, T., Becker, W., Walter, U.: Timing X-ray pulsars with application to spacecraft navigation. In: *High-time resolution astrophysics IV. Proceedings of Science*. [arXiv:1011.5095v1](https://arxiv.org/abs/1011.5095v1) (2010) Accessed 23 August (2013)
11. Bloch, M., Mancini, O., McClelland, T.: Effects of radiation on performance of space-borne quartz crystal oscillators. In: *Proceedings of European Frequency and Time Forum, Besancon, France*, pp. 171–174, 20–24 April (2009)
12. Camilo, F., Lorimer, D.R., Bhat, N.D.R., Gotthelf, E.V., Halpern, J.P., Wang, Q.D., Lu, F.J., Mirabal, N.: Discovery of a 136 millisecond radio and X-Ray pulsar in supernova remnant G54.1 + 0.3. *Astrophys. J.* **574**, L71–L74 (2002)
13. Chatterjee, S., Gaensler, B.M., Melatos, A., Briskin, W.F., Stappers, B.W.: Pulsed X-Ray emission from pulsar a in the double pulsar system J0737-3039. *Astrophys. J.* **670**, 1301–1306 (2007)
14. Chester, T.J., Butman, S.A.: Navigation using X-Ray pulsars. NASA Technical Report. N81-27129, pp. 22–25. http://ipnpr.jpl.nasa.gov/progress_report/42-63/63F.PDF (1981). Accessed 23 May 2016
15. Cognard, I., Backer, D.C.: A micro-glitch in the millisecond pulsar B1821-24 in M28. *Astrophys. J.* **612**, L125–L127 (2004)
16. Cognard, I., Bourgois, G., Lestrade, J.-F., Biraud, F., Aubry, D., Darchy, B., Drouhin, J.-P.: High-precision timing observation of the millisecond pulsar PSR 1937 + 21 at nancay. *Astron. Astrophys.* **296**, 169–179 (1995)
17. Cognard, I., Bourgois, G., Lestrade, J.-F., Biraud, F., Aubry, D., Darchy, B., Drouhin, J.-P.: High-precision timing observation of the millisecond pulsar PSR 1821–24 at nancay. *Astron. Astrophys.* **311**, 179–188 (1996)
18. Curkendall, D. W., Border, J. S.: Delta-DOR: The one-nanoradian navigation measurement system of the deep space network – history, architecture and componentry. ResearchGate. http://www.researchgate.net/publication/258791759_Delta-DOR_The_One-Nanoradian_Navigation_Measurement_System_of_the_Deep_Space_Network_-_History_Architecture_and_Componentry (2013) Accessed 4 November 2015
19. Cusumano, G., Hermsen, W., Kramer, M., Kuiper, L., Löhmer, O., Massaro, E., Mineo, T., Nicastro, L., Stappers, B.W.: The phase of the radio and X-ray pulses of PSR B1937 + 21. *Astron. Astrophys.* **410**, L9 (2003)

20. De Luca, A., Caraveo, P.A., Mereghetti, S., Negroni, M., Bignami, G.F.: On the polar caps of the three musketeers. *Astrophys. J.* **623**, 1051–1069 (2005)
21. Deng, X.P., Hobbs, G., You, X.P., Li, M.T., Keith, M.J., Shannon, R.M., Coles, W., Manchester, R.N., Zheng, J.H., Yu, X.Z., Gao, D., Wu, X., Chen, D.: Interplanetary spacecraft navigation using pulsars. *Adv Space Res.* **52**(9), 1602–1621 (2013)
22. Downs, G.S.: Interplanetary navigation using pulsating radio sources. NASA Technical Report. N74-34150, pp. 1–12. <http://ntrs.nasa.gov/archive/nasa/casi.ntrs.nasa.gov/19740026037.pdf> (1974). Accessed 23 May 2016
23. Droz, F., Mosset, P., Barmaverain, G., Rochat, P., Wang, Q., Belloni, M., Mattioni, L., Schmidt, U., Pike, T., Emma, F. and Waller, P.: The on-board Galileo clocks: rubidium standard and passive hydrogen maser – current status and performance. In: Proceedings of the European Frequency and Time Forum, Braunschweig, Germany, pp. 420–426, 27–30 March (2006)
24. Emadzadeh, A. A., Speyer, J. L.: *Navigation in Space by X-ray Pulsars*. Springer Science & Business Media (2011)
25. Espinoza, C.M., Lyne, A.G., Stappers, B.W., Kramer, M.: A study of 315 glitches in the rotation of 102 pulsars. *Mon. Not. R. Astron. Soc.* **414**(2), 1679–1704 (2011)
26. Evans, I.N., Primini, F.A., Glotfelty, K.J., Anderson, C.S., Bonaventura, N.R., Chen, J.C., Davis, J.E., Doe, S.M., Evans, J.D., Fabbiano, G., Galle, E.C., Gibbs II, D.G., Grier, J.D., Hain, R.M., Hall, D.M., Harbo, P.N., He, X., Houck, J.C., Karovska, M., Kashyap, V.L., Lauer, J., McCollough, M.L., McDowell, J.C., Miller, J.B., Mitschang, A.W., Morgan, D.L., Mossman, A.E., Nichols, J.S., Nowak, M.A., Plummer, D.A., Refsdal, B.L., Rots, A.H., Siemiginowska, A., Sundheim, B.A., Tibbetts, M.S., Van Stone, D.W., Winkelman, S.L., Zografou, P.: The Chandra source catalog. *Astrophys. J.* **189**, 37–82 (2010)
27. Feroci, M., Stella, L., van der Klis, M., et al.: The large observatory for X-ray timing (LOFT). *Exp. Astron.* **34**, 415–444 (2012)
28. Fraser, G.W.: *X-ray detectors in astronomy*. Cambridge University Press, Cambridge (2009)
29. Fraser, G.W., Carpenter, J.D., Rothery, D.A., Pearson, J.F., Martindale, A., Huovelin, J., Treis, J., Anand, M., Anttila, M., Ashcroft, M., Benkoff, J., Bland, P., Bowyer, A., Bradley, A., Bridges, J., Brown, C., Bulloch, C., Bunce, E.J., Christensen, U., Evans, M., Fairbend, R., Feasey, M., Giannini, F., Hermann, S., Hesse, M., Hilchenbach, M., Jorden, T., Joy, K., Kaipainen, M., Kitchingman, I., Lechner, P., Lutz, G., Malkki, A., Muinonen, K., Näränen, J., Portin, P., Prydderch, M., Juan, J., San Sclater, S.E., Schyns, E., Stevenson, T.J., Strüder, L., Syrjasuo, M., Talboys, D., Thomas, P., Whitford, C., Whitehead, S.: The mercury imaging X-ray spectrometer (MIXS) on BepiColombo. *Planet. Space Sci.* **58**(1–2), 79–95 (2010)
30. Galloway, D.K., Markwardt, C.B., Morgan, E.H., Chakrabarty, D., Strohmayer, T.E.: Discovery of the accretion-powered millisecond X-ray pulsar IGR J00291 + 5934. *Astrophys. J.* **622**, L45–L48 (2005)
31. Golshan, A. R., Sheikh S. I.: On Pulse Phase Estimation and Tracking of Variable Celestial X-Ray Sources In: Institute of Navigation 63rd Annual Meeting. Cambridge, MA, April 23–25 (2007)
32. Gonzalez, M.E., Kaspi, V.M., Camilo, F., Gaensler, B.M., Pivovarov, M.J.: Unusual pulsed X-Ray emission from the young, high magnetic field pulsar PSR J1119-6127. *Astrophys. J.* **630**, 489–494 (2005)
33. Gotthelf, E.V., Vasisht, G., Boylan-Kolchin, M., Torii, K.: A 700 Year-old Pulsar in the Supernova Remnant Kesteven 75. *Astrophys. J.* **542**, L37–L40 (2000)
34. Graven, P., Collins, J., Sheikh, S., Hanson, J., Ray, P., Wood, K.: XNAV for Deep Space Navigation. In: 31st Annual AAS Guidance and Control Conference. 08–054, Breckenridge CO, 4 February (2008)
35. Halpern, J.P., et al.: Neutron stars in supernova remnants. *ASP Conf. Ser.* **271**, 199 (2002)
36. Hanson, J., Sheikh, S., Graven, P., Collins, J.: Noise analysis for X-ray navigation systems. In: IEEE/ION Position, Location and Navigation Symposium. pp. 704–713, 5–8 May (2008)
37. Hessels, J.W.T., Roberts, M.S.E., Ransom, S.M., Kaspi, V.M., Romani, R.W., Ng, C.Y., Freire, P.C.C., Gaensler, B.M.: Observations of PSR J2021 + 3651 and its X-Ray pulsar wind nebula G75.2 + 0.1. *Astrophys. J.* **612**, 389 (2004)
38. Hobbs, G.: Pulsars as gravitational wave detectors (2010) <http://arxiv.org/abs/1006.3969> Accessed 4 November 2015
39. Hobbs, G., Lyne, A.G., Kramer, M.: Pulsar timing noise. *Chin. J. Astron. Astrophys.* **6**(Suppl. 2), 169–175 (2006)
40. Hughes, J.P., Slane, P.O., Park, S., Roming, P.W.A., Burrows, D.N.: An X-Ray pulsar in the oxygen-rich supernova remnant G292.0 + 1.8. *Astrophys. J.* **591**, L139 (2003)
41. Iess, L., Budnik, F., Colamarino, C., Corbelli, A., Di Benedetto, M., Fabbri, V., Graziani, A., Hunt, R., James, N., Lanucara, M., Maddè, R., Marabucci, M., Mariotti, G., Mercolino, M., Racioppa, P., Simone, L., Tortora, P., Westcott, M., Zannoni, M.: Improving tracking systems for deep space navigation. ResearchGate. http://www.researchgate.net/publication/257066682_IMPROVING_TRACKING_SYSTEMS_FOR_DEEP_SPACE_NAVIGATION (2013) Accessed 22 October 2015

42. Jahoda, K., Swank, J.H., Giles, A.B., Stark, M.J., Strohmayer, T., Zhang, W., Morgan, E.H.: In-orbit performance and calibration of the Rossi X-ray timing explorer (RXTE) proportional counter array (PCA). In: Proceedings of Soc. Photo-Opt. Instru. 2808, pp. 59–70 (1996)
43. Kaaret, P., Marshall, H.L., Aldcroft, T.L., Graessle, D.E., Karovska, M., Murray, S.S., Rots, A.H., Schulz, N.S., Seward, F.D.: Chandra observations of the young pulsar PSR B0540-69. *Astrophys. J.* **546**, 1159 (2001)
44. Kaplan, E.D.: Understanding GPS Principles and Applications. Artech House (1996)
45. Kirkpatrick, P., Baez, A.V.: Formation of optical images by X-rays. *J. Opt. Soc. Am.* **38**, 766–774 (1948)
46. Lange, C., Camilo, F., Wex, N., Kramer, M., Backer, D.C., Lyne, A.G., Doroshenko, O.: Precision timing measurements of PSR J1012+5307. *Mon. Not. R. Astron. Soc.* **326**, 274 (2001)
47. Lobanov, A.P., Horns, D., Muxlow, T.W.B.: VLBI imaging of a flare in the crab nebula: more than just a spot. *Astron. Astrophys.* **533**, A10 (2011)
48. Lorimer, D., Kramer, M.: Handbook of pulsar astronomy. Cambridge University Press, Cambridge (2005)
49. Lyne, A.G., Pritchard, R.S., Graham Smith, F.: 23 years of crab pulsar rotational history. *Mon. Not. R. Astron. Soc.* **265**, 1003–1012 (1993)
50. Lyne, A.G., Smith, F.G.: Pulsar astronomy. Cambridge University Press, Cambridge (2012)
51. Majewski, P., Andricek, L., Bahr, A., De Vita, G., Gunther, B., Hermenau, K., Hilchenbach, M., Lauf, T., Lechner, P., Lutz, G., Miessner, D., Porro, M., Reiffers, J., Richter, R., Schaller, G., Schnecke, M., Schopper, F., Soltau, H., Stefanescu, A., Strecker, R., Struder, L., Treis, J.: DEPFET macropixel detectors for MIXS: integration and qualification of the flight detectors. *IEEE T. Nucl. Sci.* **59**, 2479–2486 (2012)
52. Manchester, R.N., Hobbs, G.B., Teoh, A., Hobbs, M.: The Australia telescope national facility pulsar catalogue. *Astron. J.* 129, 1993–2006 (2005). <http://www.atnf.csiro.au/research/pulsar/psrcat> Accessed 22 October 2015
53. Martin-Carrillo, A., Kirsch, M.G.F., Caballero, I., et al.: The relative and absolute timing accuracy of the EPIC-pn camera on XMM-newton, from X-ray pulsations of the crab and other pulsars. *Astron. Astrophys.* **545**, A126 (2012)
54. Martindale, A., Pearson, J. F., Fraser, G. W., Carpenter, J. D., Willingale, R., Stevenson, T., Whitford, C., Giannini, F., Fairbend, R., Seguy, J., Sclater, E., Delgado, I., Kaipiainen, M., Nenonen, S., Pilvi, T., Schyns, E., Bulloch, C., Sawyers, C., Muinonen, K.: The Mercury Imaging X-ray Spectrometer: optics design and characterisation. In: Proceedings of Soc. Photo-Opt. Instru. 7441 (2009)
55. McGowan, K.E., Kennea, J.A., Zane, S., Córdova, F.A., Cropper, M., Ho, C., Sasseen, T., Vestrand, W.T.: Detection of pulsed X-Ray emission from XMM-newton observations of PSR J0538+2817. *Astrophys. J.* **591**, 380–387 (2003)
56. McGowan, K.E., Zane, S., Cropper, M., Kennea, J.A., Córdova, F.A., Ho, C., Sasseen, T., Vestrand, W.T.: XMM-newton observations of PSR B1706-44. *Astrophys. J.* **600**, 343–350 (2004)
57. Murray, S.S., Slane, P.O., Seward, F.D., Ransom, S.M., Gaensler, B.M.: Discovery of X-Ray pulsations from the compact central source in the supernova remnant 3C 58. *Astrophys. J.* **568**, 226–231 (2002)
58. Nicastro, L., Cusumano, G., Löhmer, O., Kramer, M., Kuiper, L., Hermesen, W., Mineo, T., Becker, W.: BeppoSAX observation of PSR B1937+21. *Astron. Astrophys.* **413**, 1065–1072 (2004)
59. Parkinson, B. W.: GPS Error Analysis. In: Parkinson, B. W., Spilker, J.J. (eds.) *Global Positioning System: Theory and Applications Volume 1*, pp. 469–484. American Institute of Aeronautics, Inc. (1996)
60. Porro, M.: Development of the DEPFET sensor with signal compression: A large format X-ray imager with mega-frame readout capability for the European XFEL. Nuclear Science Symposium and Medical Imaging Conference (NSS/MIC), pp. 1424–1434 (2011)
61. Ptak, A., Griffiths, R.: XAssist: a system for the automation of X-ray astrophysics analysis in: ADASS XII. *ASP Conf Ser.* **295**, 465 (2003)
62. Ray, P.S., Sheikh, S. I., Graven, P. H., Wolff, M. T., Wood, K. S., Gendreau.: Deep space navigation using celestial X-ray sources. In: Proceedings of the Institute of Navigation, National Technical Meeting, San Diego, CA. pp. 101–109, 28–30 January (2008)
63. Reichley, P., Downs, G., Morris, G.: Use of pulsar signals as clocks. NASA Jet Propulsion Laboratory Quarterly Technical Review. 1, 2, pp. 80–86 <http://ntrs.nasa.gov/archive/nasa/casi.ntrs.nasa.gov/19710021630.pdf> (1971). Accessed 15 May 2016
64. Roberts, S.E., Romani, R.W., Johnston, S.: Multiwavelength studies of PSR J1420-6048, a young pulsar in the kookaburra. *Astrophys. J.* **561**, L187–L190 (2001)
65. ROSAT Consortium.: ROSAT Source Catalogues. *ROSAT News.* 74 (2001)
66. Rots, A.H., Jahoda, K., Macomb, D.J., Kawai, N., Saito, Y., Kaspi, V.M., Lyne, A.G., Manchester, R.N., Backer, D.C., Somer, A.L., Marsden, D., Rothschild, R.E.: ROSSI X-ray timing explorer absolute timing results for the pulsars B1821-24 and B1509-58. *Astrophys. J.* **501**, 749–757 (1998)

67. Schiller, S., Gorlitz, A., Nevsky, A., Alighanbari, S., Vasilyev, S., Abou-Jaoudeh, C., Mura, G., Franzen, T., Sterr, U., Falke, S., Lisdar, C., Rasel, E., Kulosa, A., Bize, S., Lodewyck, J., Tino, G. M., Poli, N., Schioppa, M., Bongs, K., Singh, Y., Gill, P., Barwood, G. P., Ovchinnikov, Y. B., Stuhler, J., Kaenders, W., Braxmaier, C., Holzwarth, R., Donati, A., Lecomte, S., Calonico, D., Levi, F.: The space optical clocks project: development of high-performance transportable and breadboard optical clocks and advanced subsystems. In: Proceedings of the European Frequency and Time Forum, Gothenburg, Sweden, pp. 412–418, 24–26 April (2012)
68. Sheikh, S. I., Golshan, A. R., Pines, D. J.: Absolute and Relative Position Determination Using Variable Celestial X-ray Sources. In: 30th Annual AAS Guidance and Control Conference. pp. 855–874, 3–7 February (2007)
69. Sheikh, S.I., Pines, D.J., Wood, K.S., Ray, P.S., Lovellette, M.N., Wolff, M.T.: Spacecraft navigation using X-ray pulsars. *J. Guid. Control. Dynam.* **29**(1), 49–63 (2006)
70. Sheikh, S. I., Ray, P. S., Weiner, K., Wolff, M. T., Wood, K. S.: Relative Navigation of Spacecraft Utilizing Bright, Aperiodic Celestial Sources, In: Institute of Navigation 63rd Annual Meeting. Cambridge, MA, 23–25 April (2007)
71. Shemar, S.L., Lyne, A.G.: Observations of pulsar glitches. *Mon. Not. R. Astron. Soc.* **282**, 677–690 (1996)
72. Tjoelker, R. L., Burt, E. A., Chung, S., Hamell, R. L., Prestage, J. D., Tucker, B., Cash, P., Lutwak, R.: Mercury atomic frequency standards for space based navigation and time-keeping. In: Proceedings of the 43rd Annual Precise Time and Time Interval Systems and Applications Meeting, Long Beach, California, pp. 293–304, 14–17 November (2011)
73. Torii, K., Saito, Y., Nagase, F., Yamagami, T., Kamae, T., Hirayama, M., Kawai, N., Sakurai, I., Namiki, M., Shibata, S., Gunji, S., Finley, J.P.: ASCA detection of pulsed X-Ray emission from PSR J0631 + 1036. *Astrophys. J.* **551**, L151–L154 (2001)
74. Torii, K., Tsunemi, H., Dotani, T., Mitsuda, K., Kawai, N., Kinugasa, K., Saito, Y., Shibata, S.: Spin-down of the 65 millisecond X-Ray pulsar in the supernova remnant G11.2-0.3. *Astrophys. J.* **523**, L69–L72 (1999)
75. Verbiest, J.P.W., Bailes, M., van Straten, W., Hobbs, G.B., Edwards, R.T., Manchester, R.N., Bhat, N.D.R., Sarkissian, J.M., Jacoby, B.A., Kulkarni, S.R.: Precision timing of PSR J0437-4715: an accurate pulsar distance, a high pulsar mass and a limit on the variation of Newton's gravitational constant. *Astrophys. J.* **679**, 675–680 (2008)
76. Voges, W., Aschenbach, B., Boller, T., Braeuninger, H., Briel, U., Burkert, W., Dennerl, K., Englhauser, J., Gruber, R., Haberl, F., Hartner, G., Hasinger, G., Pfeffermann, E., Pietsch, W., Predehl, P., Rosso, C., Schmitt, J., Truemper, J., Zimmermann, H.: The ROSAT all-sky survey bright source catalogue. *Astron. Astrophys.* **349**, 389–405 (1999)
77. Voges, W., Aschenbach, B., Boller, T., Braeuninger, H., Briel, U., Burkert, W., Dennerl, K., Englhauser, J., Gruber, R., Haberl, F., Hartner, G., Hasinger, G., Pfeffermann, E., Pietsch, W., Predehl, P., Schmitt, J., Truemper, J., Zimmermann, U.: ROSAT All-Sky survey faint source catalog. *IAU Circ.* 7432, 1 (2000)
78. Watson, M.G., Schroeder, A.C., Fyfe, D., Page, C.G., Lamer, G., Mateos, S., Pye, J., Sakano, M., Rosen, S., Ballet, J., Barcons, X., Barret, D., Boller, T., Brunner, H., Brusa, M., Caccianiga, A., Carrera, F.J., Ceballos, M., Della Ceca, R., Denby, M., Denkinson, G., Dupuy, S., Farrell, S., Frascchetti, F., Freyberg, M.J., Guillout, P., Hambaryan, V., Maccacaro, T., Mathiesen, B., McMahon, R., Michel, L., Motch, C., Osborne, J.P., Page, M., Pakull, M.W., Pietsch, W., Saxton, R., Schwobe, A., Severgnini, P., Simpson, M., Sironi, G., Stewart, G., Stewart, I.M., Stobbart, A., Tedds, J., Warwick, R., Webb, N., West, R., Worrall, D.Y.: The XMM-newton serendipitous survey. V. The second XMM-newton serendipitous source catalogue. *Astron. Astrophys.* **493**, 339–373 (2009)
79. Webb, N.A., Olive, J.-F., Barret, D., Kramer, M., Cognard, I., Löhmer, O.: XMM-newton spectral and timing analysis of the faint millisecond pulsars PSR J0751 + 1807 and PSR J1012 + 5307. *Astron. Astrophys.* 419, 269 (2004)
80. Weisberg, J.M., Taylor, J.H.: Observations of post-Newtonian timing effects in the binary pulsar PSR 1913 + 16. *Phys. Rev. Lett.* **52**, 1348–1350 (1984)
81. Willingale, R., Fraser, G.W., Brunton, A.N., Martin, A.P.: Hard X-ray imaging with microchannel plate optics. *Exp. Astron.* **8**, 281–296 (1998)
82. Zane, S., Walton, D., Kennedy, T., et al.: The large area detector of LOFT: the Large Observatory for X-ray Timing. In: Proceedings of Soc. Photo-Opt. Instrum. 9144, Space Telescopes and Instrumentation, Quebec, Canada, id. 91442 W, 22 June (2014)
83. Zavlin, V.E.: XMM-Newton observations of four millisecond pulsars. *Astrophys. J.* **638**, 951–962 (2006)
84. Zavlin, V.E.: First X-Ray observations of the young pulsar J1357-6429. *Astrophys. J.* **665**, L143–L146 (2007)